Journal of African Earth Sciences 165 (2020) 103783

Contents lists available at ScienceDirect

Journal of African Earth Sciences

journal homepage: www.elsevier.com/locate/jafrearsci

Metamorphic and metasomatic evolution of the Western Domain of the Karagwe-Ankole Belt (Central Africa)

Johanna Van Daele[a,*], Niels Hulsbosch[a], Stijn Dewaele[b], Philippe Muchez[a]

[a] KU Leuven, Geodynamics and Geofluids Research Group, Department of Earth and Environmental Sciences, Celestijnenlaan 200E, 3001, Leuven, Belgium
[b] Ghent University, Department of Geology, Krijgslaan 281, S8, 9000, Ghent, Belgium

ARTICLE INFO

Keywords:
Barrovian metamorphism
Garnet–biotite geothermometry
Chlorite geothermometry
Amphibolite facies
Greenschist facies

ABSTRACT

The tectonometamorphic evolution of the Western Domain of the Karagwe-Ankole Belt, containing widespread granite-related W–Nb–Ta–Sn mineralization in pegmatites and hydrothermal quartz veins of Early Neoproterozoic age, is largely unknown. This study aims to characterize the Meso- and Neoproterozoic metamorphism and metasomatism in the Karagwe-Ankole Belt, to reconstruct the temperature evolution and to investigate its temporal relation to deformation and the widespread granite magmatism and mineralization. A quantitative geothermometric study was conducted on metasiltstones and amphibolites, and applies thin section petrography, garnet–biotite and chlorite geothermometry on samples collected in the representative Kibuye-Gitarama-Gatumba area in West Rwanda. The presence of garnet, staurolite and kyanite in metasiltstones, and hornblende and andesine-labradorite feldspar in amphibolites indicates prograde Barrovian metamorphism up to syn-to post-deformational (D1 or D2) lower amphibolite facies (up to 630 °C). This peak metamorphism was followed by post-D2 greenschist facies metamorphism (*c.* 525 °C–440 °C; garnet, biotite, chlorite, muscovite in metasiltstone), probably related to the East African Orogeny as part of the Gondwana assembly. A geothermometric evolution with high temperature conditions (> 500 °C) at least from the flare-up of Early Neoproterozoic tin granites and their metasomatic haloes onwards for most of the Neoproterozoic is proposed, in close correspondence with the geodynamic evolution of the neighboring terranes. Additionally, this high temperature regime is an important factor to be taken into account when interpreting thermal diffusion-sensitive geochronological data.

1. Introduction

The Karagwe-Ankole Belt (KAB) is an orogenic belt located in Central Africa, covering the countries Rwanda and Burundi, and parts of south-western Uganda, north-western Tanzania and the former Kivu and Maniema provinces of the D.R. Congo (Fig. 1). The KAB forms the northwestern continuation of the Kibara Belt (KIB) in the D.R. Congo and is divided along the mafic – ultra-mafic Kabanga-Musongati (KM) alignment in a Western Domain (WD) with Paleoproterozoic basement and an Eastern Domain (ED) with Archean basement, each representing independent sub-basin(s) (Fig. 1a; Tack et al., 1994). Sediments in these intracratonic KAB basins were deposited between 1420 Ma and 986 Ma (Fernandez-Alonso et al., 2012). Together, the Mesoproterozoic KAB and KIB were previously defined as the Kibaran Belt *sensu lato* (Tack et al., 2010). Although they show similarities in sedimentation, magmatism and deformation histories, they are structurally separated from each other by the uplifted, NW-trending Rusizi-Ubende Belt (Fig. 1b).

Multiple geodynamic models have been proposed for these two belts during the Meso- and Neoproterozoic (Kokonyangi et al., 2007; De Waele et al., 2008; Tack et al., 2010; Fernandez-Alonso et al., 2012; Debruyne et al., 2015; Koegelenberg et al., 2015). Generally, the KAB is interpreted to have developed in the Mesoproterozoic extension–compression setting of the proto-Congo Craton, that existed as one coherent entity since 1375 Ma, possibly even since 1.8 Ma (e.g. De Waele et al., 2008; Fernandez-Alonso et al., 2012; Klerkx et al., 1984; Tack et al., 2010). Other studies favor a subduction–collision setting in the KAB during the Mesoproterozoic, as generally proposed for the KIB (e.g. Debruyne et al., 2015; Koegelenberg and Kisters, 2014; Kokonyangi et al., 2005, 2004, 2006; Pohl, 1988). In both scenarios, compressional deformation took place at the start of the Neoproterozoic, influenced by the distant Irumide Belt formation in Zambia and Malawi as part of the Rodinia amalgamation (Fig. 1b; Fernandez-Alonso et al., 2012). This event was closely followed by important granite-related mineralization in the WD of the KAB. Granite-related Nb–Ta–Sn

* Corresponding author.
E-mail address: johanna.vandaele@kuleuven.be (J. Van Daele).

https://doi.org/10.1016/j.jafrearsci.2020.103783
Received 30 October 2019; Received in revised form 27 January 2020; Accepted 3 February 2020
Available online 08 February 2020
1464-343X/

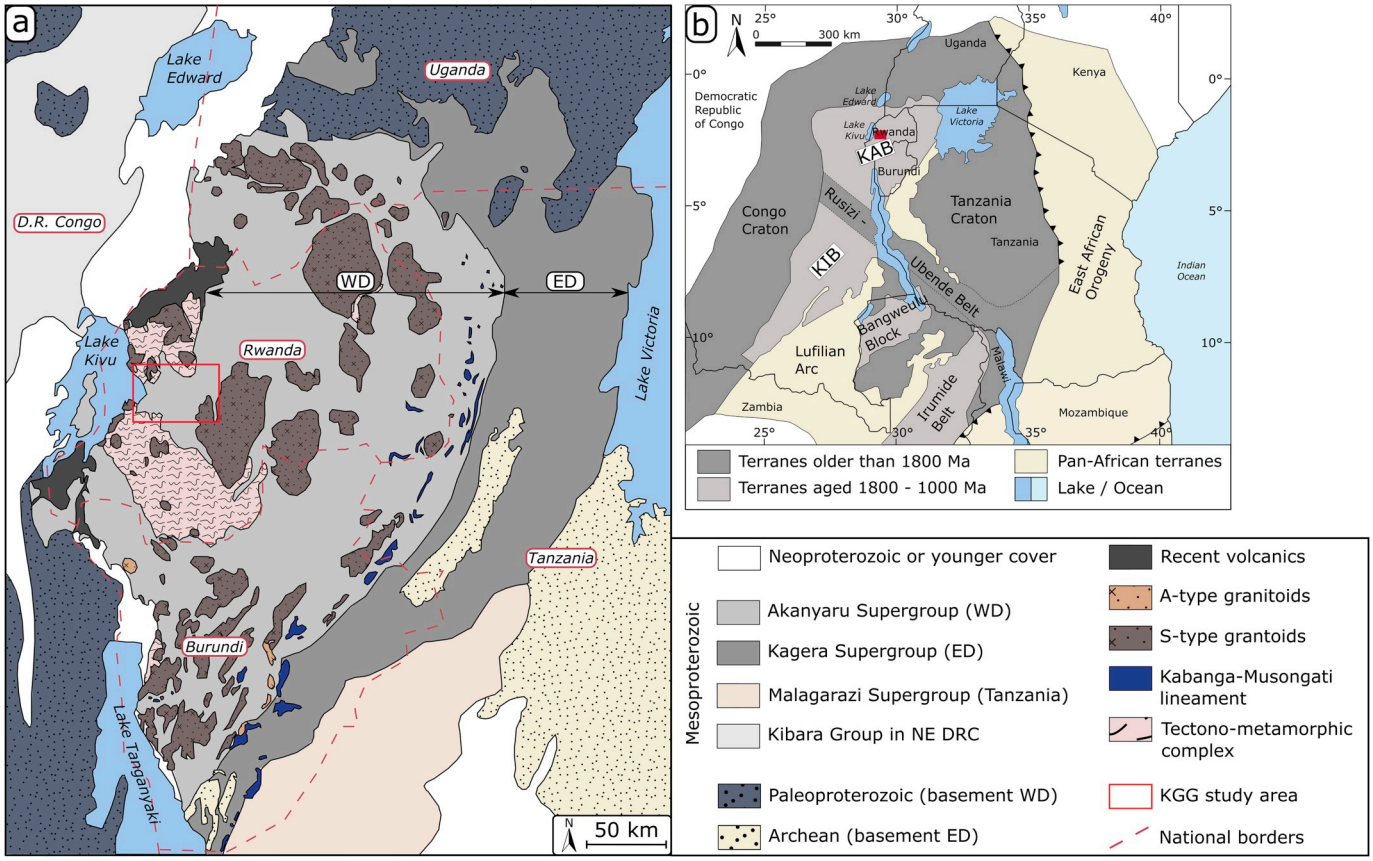

Fig. 1. (a) Geological setting of the Karagwe-Ankole Belt. Modified from Koegelenberg and Kisters (2014). (b) Geological setting of Central Africa. Modified from Dewaele et al. (2011). The Kibuye-Gitarama-Gatumba study area in West-Rwanda is indicated in red. WD = Western Domain, ED = Eastern Domain, KIB = Kibaran Belt, KAB = Karagwe-Ankole Belt. (For interpretation of the references to color in this figure legend, the reader is referred to the Web version of this article.)

mineralized LCT-pegmatites and W- or Sn-bearing quartz veins were emplaced in the period between 998 and 957 Ma (e.g. Brinckmann et al., 2001; Dewaele et al., 2011, 2016; Melcher et al., 2015). These mineralization have been related to extreme fractional crystallization (pegmatites), fluid exsolution and fluid mixing (hydrothermal quartz veins) (Hulsbosch et al., 2016, 2014; Van Daele et al., 2018a). Around 550 Ma, a NS-oriented Pan-African deformational overprint was recorded in the KAB, and has been related to the East African Orogeny during the Gondwana amalgamation (Dewaele et al., 2011; Fernandez-Alonso et al., 2012). However, the external far-field character of the two Neoproterozoic deformation events (at *c.* 1000 and *c.* 550 Ma) was challenged based on the regional-scale geometry, kinematic structures and metamorphic zonation of the belt (Koegelenberg and Kisters, 2014). Additionally, a Neoproterozoic metamorphic episode has been dated in the KAB at 966 ± 11 Ma (SHRIMP U–Pb age of metamorphic zircon rim; Tack et al., 2010) and 962 ± 7 Ma (U–Pb garnet in metamorphosed G4-granite; de Kock et al., 2014), of which the origin and relation to these deformational events has not been determined yet.

Hence, the Neoproterozoic deformational and metamorphic history of the KAB, as well as its relation to and impact on the Early Neoproterozoic mineralization is far from well-understood. In addition, multiple geochronological studies show disperse, mostly Neoproterozoic ages ranging from 1082 to 486 Ma (Cahen et al., 1984; Dewaele et al., 2011 (U–Pb on columbite-tantalite, Ar–Ar on muscovite); Van Daele et al., 2018b (Rb–Sr and Ar–Ar on phyllosilicates)), to which up-to-date no specific geological events could be connected. Previous research in the KAB mainly focused on the sedimentological and structural features of metasediments, as well as on the Mesoproterozoic igneous bodies and their associated mineralization, but only limited studies have been done to quantitatively reconstruct the tectonometamorphic and geothermometric evolution of the KAB. Furthermore, to our knowledge, a detailed minero-chemical investigation of the metasediments, representing the dominant part of the lithological record, is lacking. Yet, such results provide important insights in the metamorphic history and temperature evolution of the Karagwe-Ankole Belt.

This study aims to define the temperature evolution during the Meso- and Neoproterozoic metamorphic and metasomatic events in the Karagwe-Ankole Belt in order to evaluate if and how these aspects relate to the disperse geochronological record and have influenced the mineralization. In order to do so, this manuscript discusses results of a detailed petrographic, paragenetic and geothermometric study on representative samples from the Kibuye-Gitarama-Gatumba (KGG; Fig. 1a). Outcrops of all lithologies in the WD of the KAB (metasiltstone, metasandstone, mafic and felsic intrusions, and pegmatite) are represented in the KGG area in Western Rwanda. Additionally, this area allows a clear comparison in terms of mineral assemblages and temperature evolution between areas with abundant granite and pegmatite intrusions (Gatumba-Gitarama) and areas where these are absent (Kibuye). Consequently, the KGG area provides a unique opportunity to gain knowledge on the metamorphic evolution in the Western Domain of the Karagwe-Ankole Belt, and to explore the link with the observed scattered geochronological record.

2. Geological setting

2.1. Geological setting of the Western Domain of the Karagwe-Ankole Belt

The Mesoproterozoic Karagwe-Ankole Belt (KAB) is located between two Paleoproterozoic – Archean cratons, the Tanzania Craton in the

east and the Congo Craton in the west. This belt is divided in two domains: the Eastern Domain (ED) with an Archean basement and the Western Domain (WD) with a Paleoproterozoic basement (Tack et al., 1994, Fig. 1a). During the Mesoproterozoic, this basement was covered by terrigenous shallow-water sediments (Buchwaldt et al., 2008; Tack et al., 2010; Fernandez-Alonso et al., 2012). The sedimentary record dominantly consists of siliciclastics, ranging from fine metasiltstone to coarse metasandstone and quartzite. These sediments are part of the Akanyaru Supergroup, which contains four groups: the Gikoro, Pindura, Cyohoha and Rugezi groups (from old to young). Although no unconformity was observed in the field, two distinct sedimentation periods are proposed based on geological mapping and detrital zircon populations (Fernandez-Alonso et al., 2012). The first sedimentation period, which took place between 1.42 and 1.37 Ga, comprises the Gikoro and Pindura groups and has an estimated total thickness of *c.* 15 km (Fernandez-Alonso et al., 1986, 2012). After a regional hiatus and erosion phase, the Cyohoha and Rugezi groups were deposited from 1220 Ma onwards. Geochronology of G4 granites indicates deposition ceased prior to 986 ± 10 Ma (Tack et al., 2010; Fernandez-Alonso et al., 2012).

Three main magmatic episodes, mainly intrusive, were distinguished in the KAB (Klerkx et al., 1984; Tack et al., 2010). Firstly, the oldest Mesoproterozoic metasediments (Gikoro and Pindura groups) were intruded by widespread bimodal magmatism at *c.* 1375 Ma (Tack et al., 2010). Mafic – ultra-mafic, Bushveld-type intrusions that occur in the Kabanga-Musongati (KM) alignment at the boundary zone between the WD and ED represent the mafic endmember. The felsic endmember (only in the WD) consists on the one hand of abundant peraluminous biotite-rich S-type granitoids, that are often strongly foliated and called the 'G1-G3 granites' in Rwanda, and on the other hand of small dolerite sills and dykes. Secondly, around 1205 Ma, A-type granite bodies were emplaced along NS-oriented shear zones (Tack et al., 2010). Lastly, Sn-bearing, S-type leucogranites, also called 'Sn granites' or 'G4-granites' in Rwanda, intruded the Mesoproterozoic metasediments and previous generations of intrusive rocks (Rumvegeri, 1991; Tack et al., 2010). This granitic magmatism has not been dated in Rwanda, but associated mineralized pegmatites in the Gatumba area have ages ranging between 998 and 966 Ma (U–Pb on columbite-tantalite and cassiterite; Dewaele et al., 2011; Melcher et al., 2015; Zhang et al., 2016). Furthermore, G4-granite associated, W-mineralized quartz veins have ages of 992–984 Ma (Ar–Ar on muscovite; De Clercq, 2012; Dewaele et al., 2016), while Sn-mineralized quartz veins are dated between 965 and 957 Ma (Rb–Sr on muscovite and U–Pb on cassiterite; Monteyne-Poulaert et al., 1962; Zhang et al., 2016).

Low-angle, bedding or layer-parallel fabrics, usually not related to folding, are omnipresent in the WD, and are most intensely developed in the Gikoro–Pindura Group metasediments (Klerkx et al., 1984, 1987; Fernandez-Alonso and Theunissen, 1998; Fernandez-Alonso et al., 2012). In addition, a discrete, oblique axial planar fabric can be observed throughout the KAB, associated with regional NW–SE to NNE–SSW trending, upright folding (Klerkx et al., 1984, 1987; Rumvegeri, 1991; Fernandez-Alonso and Theunissen, 1998; Fernandez-Alonso et al., 2012). The composite granite bodies are present in the anticlinal cores of these folds (Fernandez-Alonso et al., 2007). A third structural feature are subvertical, NE/NW-trending shear zones, resulting in multiple, shear-bounded tectonostratigraphic domains (Klerkx et al., 1984, 1987; Rumvegeri, 1991; Fernandez-Alonso and Theunissen, 1998). No geochronological studies have been performed yet to constrain the timing of deformation in the Western Domain. Fabric and strain intensity and complexity generally increase from east to west throughout the KAB and around the granite bodies (Klerkx et al., 1984, 1987; Koegelenberg and Kisters, 2014).

Previous petrographic studies have indicated that the regional metamorphism in the KAB is characterized by an increase in grade from east to west with locally developed contact-aureoles around the granite bodies as well (Klerkx et al., 1987; Rumvegeri, 1991; Koegelenberg and Kisters, 2014). The metasediments of the WD were affected by greenschist to amphibolite facies syn-kinematic Barrovian metamorphism (Deblond et al., 2001; Tack et al., 2010). In NW Burundi, mineral assemblages, garnet-biotite geothermometry and garnet-muscovite-plagioclase-biotite geobarometry indicate amphibolite peak metamorphic conditions around 520–600 °C and 4–4.8 kbar (Nahimana, 1988). Rumvegeri (1991) broadly estimated the peak P-T conditions in the eastern Kivu region at 350–800 °C and 4–8 kbar by quantitative thermobarometry. Contact metamorphic aureoles are associated with both the S-type granites and (ultra-)mafic Kabanga-Musongati intrusions (Tack et al., 2010). Retrograde metamorphism towards greenschist facies conditions (Rumvegeri, 1991) and metasomatically-induced sericitization and chloritization have also been observed (Nahimana, 1988; Börker and Pupp, 2014).

2.2. Geological setting of the Kibuye-Gitarama-Gatumba study area

Sediments in the Kibuye-Gitarama-Gatumba area (KGG area) belong to the Gikoro (Bumbogo and Ndiza formations), Pindura (Cyurugeyo Formation) and Cyohoha (Gatwaro and Sakinyaga formations) groups of the Akanyaru Supergroup (Fig. 2). Pale brown to grey metasiltstone to fine metasandstone is the most common lithology in the KGG area. Only the youngest Sakinyaga Formation dominantly consists of brown or white metasandstone and quartzite. These metasediments have been intruded by abundant dolerite sills and dykes, especially around the cities of Kibuye and Gatumba. Two large G1-G3 and G4 granite composite complexes associated with abundant pegmatites are present in the eastern part of the study area, the Gitarama batholith in the SE and the Bijojo granite in the northern Gishwati Complex. In the Kibuye area, such complexes are not present in outcrop. The small Mara and Bisesero granites southwest of Kibuye are not associated with extensive pegmatite fields as observed around Gatumba (Fig. 2; Dehandschutter et al., 1988; Fernandez-Alonso et al., 2012; Tahon et al., 1988a, 1988b).

In the KGG area abundant N–S to NW–SE-oriented folds are present, corresponding to the general structural grain of the KAB (Dehandschutter et al., 1988; Tahon et al., 1988a, 1988b). Most faults observed are inverse faults, steep and NS-oriented, such as the east over west reverse faulting in the Satinsyi complex situated west of Gatumba (Fig. 2; Fernandez-Alonso and Theunissen, 1998). Normal faulting has been observed occasionally, but is interpreted as reactivation in an extensional regime (Dehandschutter et al., 1988; Tahon et al., 1988a, 1988b; Tack et al., 2010). The anomalous NW–SE structures around Kibuye have been interpreted to have formed in a sinistral strike-slip environment (Fernandez-Alonso and Theunissen, 1998).

The assemblage muscovite–biotite–garnet(–chlorite–chloritoid ± staurolite) is interpreted as representing the regional metamorphism of the metasediments in the Kibuye-Gitarama-Gatumba area. Chlorite-rich schists are interpreted as metamorphosed volcanic or volcano-sedimentary rocks, while mafic sills are often amphibolitized (Dehandschutter et al., 1988; Tahon et al., 1988a, 1988b). Contact metamorphism occurs around granite intrusions, while 'contact' hornfels rocks are seldom observed (Tahon et al., 1988a, 1988b). Observed contact metamorphic minerals are andalusite and chiastolite (Dehandschutter et al., 1988).

In the Satinsyi complex, the rocks were affected by more intense metamorphic and metasomatic effects (Tahon et al., 1988a, 1988b). Metapelites in the Satinsyi complex occur not only as phyllites, but also as sericitoschists (Tahon et al., 1988b). Other hydrothermal effects on the metasediments resulted in silicification, tourmalinization and Li-mica formation. Pegmatite bodies are surrounded by biotite and quartz–tourmaline, often albitized schists (Gérards, 1965; Börker and Pupp, 2014). Biotite–chlorite schists, quartzites and greenschists were observed near the, to amphibolite metamorphosed, doleritic rocks (Börker and Pupp, 2014).

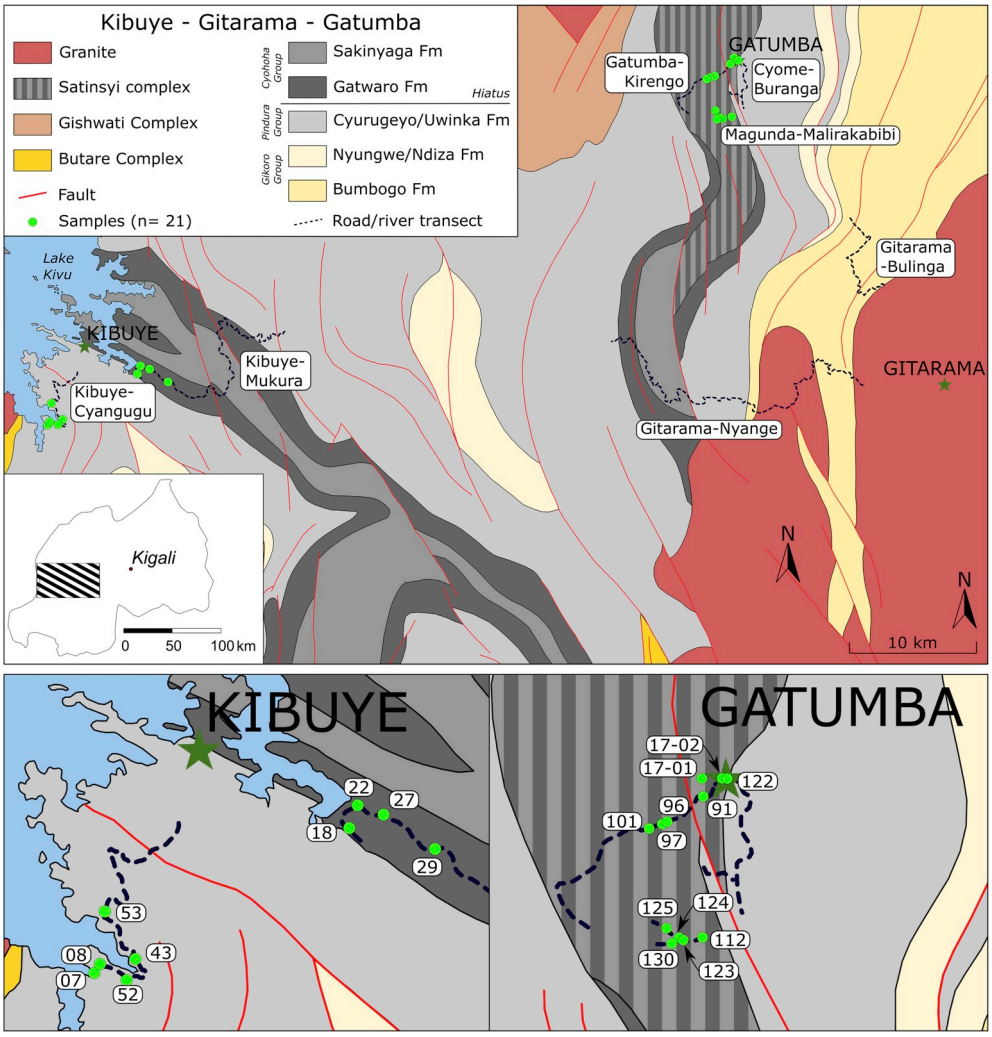

Fig. 2. Geological map of the Kibuye-Gitarama-Gatumba area (based on Dehandschutter et al., 1988; Tahon et al., 1988a, b). Road and river transects mapped and sampled during the 2016 and 2018 field campaigns are indicated with black dashed lines. Samples used in the geothermometric study are indicated with green dots. (For interpretation of the references to color in this figure legend, the reader is referred to the Web version of this article.)

3. Petrography

Multiple road and river sections were mapped during two field campaigns in the Kibuye-Gitarama-Gatumba area (Fig. 2). Representative samples were taken of all observed metamorphic and metasomatic assemblages. Approximately 100 thin sections were prepared and studied to characterize these assemblages on microscale. The samples investigated belong to the Gikoro, Pindura and Cyohoha groups. In the stratigraphy of Fernandez-Alonso et al. (2012), the first two groups are placed older than the 1375–1220 Ma hiatus, the third one occurs above the hiatus (Fig. 2). Nevertheless, no pronounced differences in terms of deformation intensity, mineral assemblage or metamorphic grade were observed between these groups. Therefore, the petrography section below gives the observations per area, and not per lithology.

3.1. Kibuye area

In the Kibuye area, two large road sections were mapped. The first is a NS-transect in the Cyurugeyo Formation from Kibuye towards Cyangugu. The second, EW–NS–EW oriented transect goes from Kibuye in direction of Mukura and crosses the Gatwaro, Sakinyaga and Cyurugeyo formations (Fig. 2).

3.1.1. Metasediments: lithology and mineralogy

The Cyurugeyo Formation is characterized by a fine metasandstone to metasiltstone lithology. Beds of quartzite occasionally occur. The dominant color varies between pale brown (the coarser beds) and dark grey (the finer beds, as in Fig. 3a). Often fine color laminations are present. Locally, boudinaged black shaley layers were observed. Towards the top of this formation, blue-grey metasiltstones constitute the dominant lithology (Fig. 3b), with a few garnet-rich, strongly folded tuff intercalations. The Gatwaro Formation is dominated by alternating beds of metasiltstone and metasandstone. These metasediments are either characterized by typical, mm-scale color laminations (pale white and brown-beige; Fig. 3c) or by a homogeneous light grey to brown or sometimes greenish color. Some intercalations of more competent metasandstone and quartzite were observed, as well as occasionally blueish metapelitic intercalations. Towards the top, except for one thick sequence of massive brown metasandstone, mostly metasiltstone and metapelite occur. Multiple white, fine, clayish layers were observed, which are interpreted as weathered tuff layers (see Dehandschutter et al., 1988). Small (oxidized) pyrite crystals with diameters between 0.5 and 1 mm are occasionally present in the Gatwaro Formation. The Sakinyaga Formation is the youngest formation present in the study area. This formation consists dominantly of hard metasandstone to massive quartzite. Again, two colors predominate: brownish with mm-scale alternations of darker and paler bands and homogeneous white.

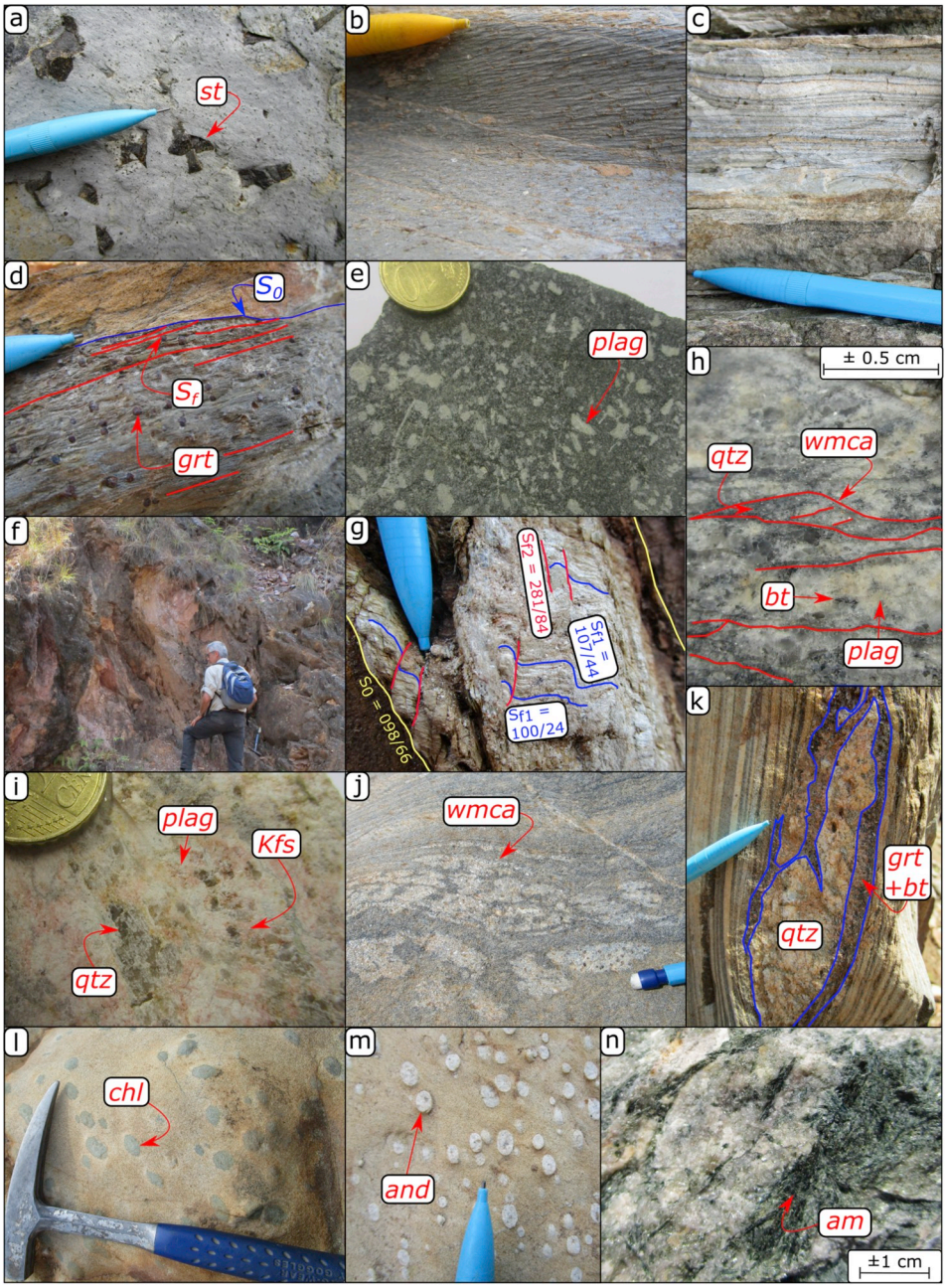

Fig. 3. Field work and handsample pictures. (**a**) Staurolite twin crystals in grey metasiltstone of the Cyurugeyo Formation (KG43). (**b**) Blue-grey metasiltstone of the Cyurugeyo Formation. (**c**) Fine color laminations in metasiltstone of the Gatwaro Formation. (**d**) Dispersed garnet porphyroblasts in grey, foliated metasiltstone. (**e**) Feldspar phenocrysts in ortho-amphibolite (KG52). (**f**) Weathered outcrops in the Gitarama transects. (**g**) Crenulated white mica schist and brown metasiltstone in the Bumbogo Formation. (**h**) Foliated biotite granite. (**i**) Unfoliated leucogranite. (**j**) Gneissic metasiltstone with abundant, elongated white mica lenses. (**k**) Gneissic metasiltstone with ellipsoidal quartz lens, rimmed by garnet-biotite zone (KG101). (**l**) Chlorite nests in light brown metasandstone of the Gatwaro Formation. (**m**) Andalusite nodules in metasiltstone of the Gatwaro Formation. (**n**) Amphibole needles in quartzite of the Sakinyaga Formation, close to diorite intrusion. Mineral abbreviations according to Siivola and Schmid (2007). (For interpretation of the references to color in this figure legend, the reader is referred to the Web version of this article.)

Intercalations of blue-grey metapelites or beige, finely laminated siltstones are occasionally present.

The matrix of all metasediments in the Kibuye area dominantly consists of quartz and graphite, with crystal dimensions mostly below 100 μm and 10 μm respectively (Fig. 4a). Additional minerals regularly observed, especially in the metapelites, are white mica, biotite, chlorite, garnet, staurolite and minor kyanite, andalusite, feldspar, pyrite, ilmenite and tourmaline.

In most samples, phyllosilicates (mainly white mica) occur dispersed in the quartz matrix or are concentrated in layers, up to mm-thick, parallel to the bedding (S_0) or foliation (S_f). A strong foliation has developed in most samples, defined either by mineralogical (e.g. presence of graphite or chlorite) and crystal size alternations, or – and most often – the preferred orientation of phyllosilicate crystals (Figs. 3d, 4b-d). Mineralogical and crystal size alternations mostly developed as bedding-parallel foliation ($S_{f1} \approx S_0$), which can be burial-induced (Fig. 4d). This was sometimes also the case for the preferred phyllosilicate orientation, although this foliation more often shows an oblique orientation to the bedding (S_{f2}; Fig. 3d). This oblique foliation is parallel to the fold axial planes on hand sample to outcrop scale and hence can be interpreted as axial planar foliation. In some outcrops, a second oblique foliation generation could be distinguished (S_{f3}), however, in most samples, only one oblique, axial planar foliation (S_{f2}) was observed. Some samples rich in white mica or graphite show asymmetric crenulation foliation, developed to varying degrees (e.g. Fig. 4d). Individual crystals are often oriented parallel to S_0, S_{f1} or S_{f2} as well (Fig. 4b and c).

In metasiltstones and -sandstones, randomly oriented phyllosilicate crystals, mainly biotite and chlorite crystals (up to 200 μm), can be concentrated in cm-sized ellipsoidal nests, sometimes with a quartz center and often S_{f2}-parallel. Additionally, chlorite was observed combined with small proportions of white mica, biotite, tourmaline and plagioclase in folded thin veins (< 500 μm thick; Fig. 4a). Altered, large (up to 800 μm in length) poikiloblastic biotite and chlorite crystals are

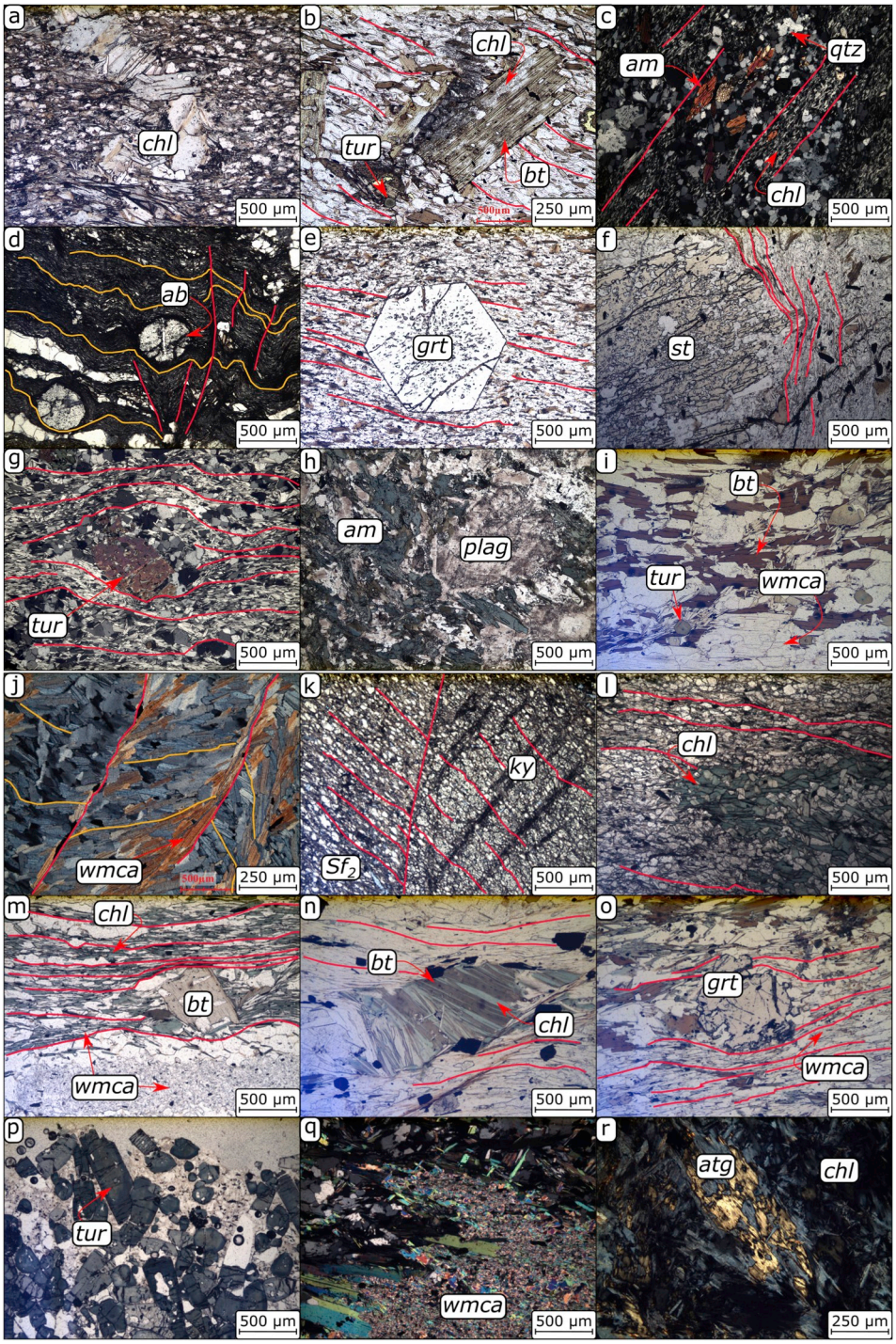

Fig. 4. Microphotographs of the Kibuye-Gitarama-Gatumba samples. Sf_1 is indicated in yellow, Sf_2 in red. (**a**) Metasiltstone KG27 with pale green chlorite in a thin, folded veinlet (ppl). (**b**) Metasiltstone KG07, chloritized biotite porphyroblast in a foliated white mica–quartz matrix, with accessory tourmaline (ppl). (**c**) Metasiltstone KG18 near amphibolite body, with abundant colorless chlorite and euhedral amphibole crystals (xpl). (**d**) Two foliations in metapelite KG61: Sf_1, defined by the presence of graphite, is crenulated by Sf_2. Albite nodules are wrapped by both foliations (ppl). (**e**) Metasiltstone KG08 with weakly developed white mica–biotite foliation and euhedral garnet porphyroblasts (ppl). (**f**) Metasiltstone KG43 with white mica foliation, biotite and large staurolite porphyroblasts (ppl). (**g**) Chlorite schist KG45 containing anhedral tourmaline crystals, which are wrapped by the chlorite foliation (xpl). (**h**) Amphibolite KG22 with sericitized feldspar and green calcic clino-amphiboles (ppl). (**i**) Fine metasandstone KG75 in contact with pegmatite body, with biotite, tourmaline and large white mica crystals (ppl). (**j**) White mica schist KG89 (see also Fig. 3g) with two white mica generations and a well-developed crenulation cleavage (xpl). (**k**) Metasiltstone KG72 with foliated kyanite porphyroblasts in a quartz–graphite–white mica matrix (ppl). (**l**) Metasiltstone KG112, chlorite aggregate in the weakly foliated quartz–white mica matrix (ppl). (**m**) Metasiltstone KG130 with elongated white mica lenses parallel to the white mica–chlorite foliation, which is disturbed by biotite porphyroblasts (ppl). (**n**) Metasiltstone KG103 with well-developed white mica foliation, partially chloritized biotite porphyroblasts and pyrite (ppl). (**o**) Metasiltstone KG125 containing anhedral garnet porphyroblasts wrapped by the white mica foliation, biotite chloritization (ppl). (**p**) Metasiltstone KG137 with abundant tourmaline crystals in the quartz–feldspar matrix (ppl). (**q**) Metasiltstone KG125 with foliation-parallel lenses containing white mica, ilmenite and little chlorite (xpl). (**r**) KG91, anhedral antigorite porphyroblasts in a matrix of colorless chlorite (xpl). Mineral abbreviations according to Siivola and Schmid (2007). (For interpretation of the references to color in this figure legend, the reader is referred to the Web version of this article.)

common and are sometimes associated with stair-stepping of S_{f1}. In the latter, biotite relicts often can be recognized (Fig. 4b).

Dispersed garnets are present in all formations, all over the study area. These porphyroblasts are generally euhedral, have a diameter of 0.5–2 mm (occasionally up to 5 mm), and show a dark-red color in fresh samples (Fig. 3d). Some garnets are oxidized or altered to biotite. In an exceptional case, quartz pressure shadows developed around garnet porphyroblasts deflecting the mica foliation S_{f2}. However, mostly garnets do not disturb the host rock foliation (Fig. 4e). Cm-size staurolite crystals were observed in grey, finely laminated metasiltstone of the Cyurugeyo Formation (Fig. 3a). These crystals are oriented parallel to the bedding or foliation but a consistent elongation was not observed. Staurolite shows its typical poikiloblastic texture in thin sections and the individual crystals deflect in all cases the matrix foliation S_{f2} (Fig. 4f).

Furthermore, relicts of diamond- and rectangular-shaped porphyroblasts were observed, interpreted to have been kyanite or staurolite. Whitish, circular lenses with a maximum diameter of 0.5 cm, sometimes with a thin black rim, were observed dispersed in chlorite schists, metasiltstone and metasandstone. These are andalusite nodules. The relation of kyanite and andalusite to the foliation could not be determined. Furthermore, circular nodules (d = 200–400 µm) consisting of albite or quartz and small white mica crystals occur, wrapped by the bedding-parallel S_{f1} (Fig. 4d). In some cases, quartz pressure shadows are present along the sides of these blasts. Lastly, small, elongated pyrite and ilmenite crystals (length of max. 50 µm) are present

dispersed in most samples. They often follow the phyllosilicate foliation S_{f2}. A minor amount of small tourmaline needles (max. d = 50 μm) was observed, occurring dispersed throughout the metasediments (e.g. Fig. 4b). In foliated rocks, the tourmaline crystals are wrapped by the foliation Sf_2 (Fig. 4g).

3.1.2. Magmatic intrusions

Felsic intrusions were not encountered in the Kibuye road transects, but mafic intrusions are frequently observed, in metasediments of both the young and old series. These mafic bodies can have a thickness up to 100 m. Smaller bodies are present as pockets, as dykes parallel to the bedding (sometimes boudinaged) or along joint planes. Mineralogically, they consist of abundant anhedral, poikiloblastic hornblende (up to 80 vol%) and feldspar crystals (Fig. 3e). Feldspar shows in most samples a bimodal crystal size distribution. It is present either as < 100 μm crystals or as macroscopic phenocrysts (Fig. 4h). Small biotite crystals and a minor amount of quartz, pyrite, epidote and apatite are present as well. Feldspar phenocrysts sometimes are slightly sericitized in the center, although saussuritization was observed as well. In some cases, the pockets deflect the host rock foliation S_{f2} or biotite and hornblende define a weak internal foliation.

3.2. Gitarama area

In the Gitarama area, two transects were mapped, mainly in the Bumbogo Formation: the EW transect going from Gitarama to Nyange and the NS transect from Gitarama to Bulinga (Fig. 2). Outcrops along these two transects are generally strongly weathered (Fig. 3f).

3.2.1. Metasediments: lithology and mineralogy

The Bumbogo Formation dominantly consists of homogeneous, light brown, fine metasilt- and sandstone and pale to grey schists. Towards the top of this formation, thick intervals of blue-grey metapelite are present. The western part of the Gitarama-Nyange transect intersects younger metasediments. The Cyurugeyo, Gatwaro and Sakinyaga formations show the same lithological characteristics as observed in the Kibuye area.

In general, quartz occurs as somewhat larger crystals than in the Kibuye area (up to 300 μm; Fig. 4i). Graphite is less, or even not present in most Gitarama samples, while dispersed white mica is significantly more abundant in the siliciclastic metasediments in the Gitarama area compared to the Kibuye area. Alternations between mica-richer and -poorer layers are frequently observed. Chlorite and biotite are also common host rock minerals. The metapelitic layers of the Bumbogo Formation often consist entirely of white mica or, more exceptionally, biotite or chlorite. In most cases, phyllosilicates define a clear, sometimes schistose, foliation oblique to the bedding. Again, this S_{f2} foliation relates to the regional fold structure observed. White mica schists, with a well-developed (asymmetric) crenulated foliation, are observed at a few outcrops of the Bumbogo Formation (Fig. 3g). This crenulation can be characterized by smooth, open folds or more abruptly kinked folds. White mica crystals and cleavage development parallel to the axial plane of this crenulation can be observed in some samples (Fig. 4j). White mica (up to 300 μm thick) and poikiloblastic biotite (up to 3 cm thick) also occur as large crystals with a random orientation. The S_{f2} foliation (if present) does not wrap around these mica crystals but is crosscut by them In some cases, biotite is chloritized.

Garnets (1–4 mm diameter) are present in the Sakinyaga and Bumbogo formations, especially in white mica and chlorite schists, but are largely oxidized. Garnets clearly wrapped by the foliation are observed in Bumbogo metapelites. Diamond-shaped kyanite porphyroblasts occur in the youngest metasediments. The host rock foliation continues in the kyanite crystals (Fig. 4k). Small, dispersed tourmaline needles (diameter up to 100 μm) and pyrite and ilmenite crystals (dimensions usually < 100 μm) occur in metapelite all over the Gitarama area. Tourmaline is considerably more abundant compared to the Kibuye area (Fig. 4b and i). Exceptionally, tourmaline needles of multiple cm large were observed in metapelites of the Bumbogo Formation. These accessory minerals do not interfere with, but often follow the crenulated foliation.

3.2.2. Magmatic intrusions

Granite and pegmatites were frequently observed in the Gitarama area. Two granite types were observed. The first type is a fine-grained, foliated granite consisting of quartz, white mica, plagioclase and (chloritized) biotite (Fig. 3h). Zircon and apatite occur as accessory minerals. Quartz and feldspar are present in a mylonitic foliation as anhedral crystals in ellipsoid lenses (few mm in size), surrounded by the white mica foliation. The second type is a leucogranite with coarse quartz, plagioclase, K-feldspar and white mica crystals. No foliation is observed in these leucogranites (Fig. 3i). Pegmatites dominantly consist of feldspar (often kaolinitized), quartz and white mica and/or biotite. They have mostly intruded along the bedding planes as observed in the Musha-Ntunga area in East Rwanda (Hulsbosch et al., 2017), but pegmatite bodies were also observed along S_{f2} or in pods in fold hinges. Host rock enclaves are sometimes present in the pegmatite body. Occasionally, mafic intrusions crosscutting the foliated granite were observed, as well as bedding-parallel sills. However, these mafic bodies are too weathered to allow a detailed mineralogical characterization.

3.3. Gatumba area

Three short transects were mapped in the Gatumba area: two river sections (Gatumba-Kirengo in the north and Magunda - Malirakabibi in the south) and one road section (Cyome-Buranga). The observations in the Gatumba area are geologically all located in the Satinsyi complex, except for the road section, which partly goes through outcrops of the Cyurugeyo Formation (Fig. 2). However, due to abundant mafic and pegmatite intrusions, its lithology could not be characterized in detail.

3.3.1. Metasediments: lithology and mineralogy

The Satinsyi complex was mapped by Tahon et al. (1988a, b) as a NS-oriented metamorphic complex, just west of the city Gatumba. On the geological map, it forms a continuum with the younger Gatwaro and Sakinyaga formations. The river section outcrops suggest that this complex indeed represents these younger formations. The fine color laminations in metasilt-to metasandstone, as well as the brownish Sakinyaga Formation metasandstone to quartzite, as observed in the Kibuye and Gitarama areas, were recognized here as well. In addition, many outcrops show rocks with a high hardness and quartzitic or gneissic texture (Fig. 3j–k).

As in the Gitarama area, dispersed white mica and intense muscovitization was frequently observed in the quartz matrix. These mica crystals are generally small, with a thickness of maximum 50 μm. Chlorite and biotite occur abundantly as well, typically as small crystals with a thickness less than 100 μm. In metasandstones, biotite and chlorite are mostly concentrated in mm-thick layers (often bedding-parallel) or in cm-size nests (Figures 3l, 4l and 4m), while metapelites can be entirely biotitized or chloritized. Phyllosilicates define in many cases a well-developed foliation (Figure 4m), but larger, randomly oriented biotite and chlorite crystals are wrapped by the host rock foliation. Chlorite, parallel to the bedding or foliation and occurring in nests, mostly has a medium green color and a clear homogeneous texture (Figures 4l and m). However, impure chlorite crystals, showing internal biotite stratifications, are present as well (Figure 4n). This is the case for large (up to 1 mm long) poikiloblastic crystals, as well as for smaller crystals following the regional foliation. The largest, often poikiloblastic crystals are not always wrapped by the host rock foliation, nor have a systematic orientation.

Small, subhedral red garnets (up to 300 μm size), sometimes biotitized, were observed. In contrast to the Kibuye area, the matrix foliation wraps around the garnet porphyroblasts (Figure 4o). Garnet can also be

found in finely laminated metasiltstones rimming quartz veins and lenses. These veins and lenses show a 0.7–1 cm thick zone enriched in biotite and garnet porphyroblasts (2–3 mm diameter; Fig. 3k). These quartz veins are often bedding-perpendicular and deformed. While they crosscut the fine host rock laminations, the host rock biotite foliation, presumably S_{f2}, is not affected by the quartz veins and thus post-date veining. Cm-sized staurolite crystals are oriented parallel to the host rock bedding, but do not show a preferential elongation, similar as has been observed in the Kibuye area.

Tourmaline is abundantly present at multiple locations, especially in the vicinity of granite and pegmatite intrusions. Tourmaline crystals occur both concentrated in layers or dispersed in the matrix but were never observed to significantly deflect the phyllosilicate foliation. The crystals reach diameters up to 500 μm and lengths of 1.5 cm (Figure 4p) and often have a distinct poikiloblastic texture. Most tourmaline crystals have a pale green to light- or dark-brown color and are unzoned. Some crystals have a more green-blue core. Additionally, large foliation-parallel and ellipsoidal white-blue lenses, largely consisting of white mica, were observed at multiple locations (Figs. 3j–4q). These white mica crystals generally are of small size but show a large size range and random orientation. Occasionally these lenses contain a minor proportion of small garnet, quartz and biotite crystals. The host rock foliation is wrapped around these lenses. Less well-defined zones with similar mineralogy were also observed in white mica schists close to pegmatite intrusions, as well as lenses consisting of coarser white mica and quartz crystals (up to 250 μm). Smaller andalusite nodules (0.5 cm diameter; Figure 3m) and kyanite are locally present, always in unfoliated rocks. Hence, it was not possible to determine their relation to the foliation. Small subhedral crystals of ilmenite and pyrite (dimensions $<$ 100 μm) occur dispersed throughout the matrix and white mica lenses.

3.3.2. Magmatic intrusions

In the Gatumba area, pegmatites and mafic intrusions are frequently observed. The pegmatites show similar mineralogical characteristics as those observed in the Gitarama area. They mostly consist of feldspar (sometimes kaolinitized), quartz, white mica and in some cases biotite or tourmaline. The mafic intrusions show an even distribution of hornblende and feldspar phenocrysts (up to 250 μm) and are generally not or only weakly foliated. Feldspars often contain patches of sericite, especially in the crystal center. Biotite occurs in varying amounts and with varying crystal sizes. Pyrite, chlorite, apatite, tourmaline and epidote are present as accessory minerals. One mafic rock sample was observed to contain antigorite in a matrix of colorless chlorite (Figure 4r).

3.4. Metasediments in contact with magmatic rocks

Metasediments situated next or close to felsic or mafic magmatic bodies show different mineralogical characteristics than those that are not located in the vicinity of these intrusions. The specific mineralogy and mineral modes in these metasediments depend both on the lithology and the type of magmatic intrusion. Metasandstones generally are less affected than metasiltstones.

Metasediments in contact with mafic intrusions are characterized by a finely crystalline chlorite-dominated mineralogy. Crystal sizes are as small as 10 μm. The chlorite typically is colorless and shows weak pleochroism (Fig. 4c). Chloritization of the host rock and pure chlorite schists with a limited amount of garnet porphyroblasts are most frequently observed. To a lesser extent, biotitization and biotite–garnet layers are associated with mafic intrusions. Biotite typically has a light to medium brown color. Other accessory minerals, not present in all samples, are amphibole (hornblende and tremolite; Fig. 4c), pyrite, white mica, quartz, plagioclase, and titanite. Pure amphibole layers or veins have been observed as well (Figure 3n). This effect on the metasediments is very local. Further away from the mafic bodies ($>$ 1.5 m), no amphibole is present while chlorite still dominates. Tourmaline was only exceptionally observed and mostly has a green-blueish tint.

Metasediments most close to pegmatites or granites (up to 20 cm distance) contain up to a few cm large white mica and quartz crystals. These crystals, especially quartz, often show kinking, subgrain development, grain boundary migration and deformation lamellae. Tourmaline was observed as well, with diameters up to 300 μm and lengths up to 1 cm. The color of the crystals varies from pale green to brown and generally shows no zoning within one crystal. Often a distinct poikiloblastic texture can be recognized. Tourmaline occurs either as dispersed crystals or concentrated in zones. In white mica schists, the crystals often define a clear foliation parallel to the granite/pegmatite – schist contact. In some cases, crenulation foliation can be recognized. This white mica and quartz (re-)crystallization effect is very intense closest to the contact, but gradually diminishes further from the pegmatite. At a distance of more than 20 cm, large white mica and quartz crystals are rare (crystal dimensions of max. 200 μm; Fig. 4g) and the metasediment foliation is fully preserved. Some granite/pegmatite – metasediment contacts are characterized by a zone (*c.* 5 cm thick) of intense biotitization, followed by the coarse white mica–quartz zone somewhat further from the contact. Biotite typical has a dark, chestnut-brown color and variable crystal sizes (20–500 μm thickness). Often, these biotite crystals define a foliation oriented parallel to the contact metasediment – intrusion (Fig. 4i). They can have a poikiloblastic texture and contain multiple very small inclusions surrounded by darker-colored, radioactive haloes, probably caused by zircon or monazite. Host rock enclaves in the pegmatites are often entirely tourmalinized or biotitized.

Where pegmatites intruded mafic rocks, the latter dominantly consist of biotite (up to $>$ 80 vol%). This zone can attain a thickness up to 50 cm and in most cases shows a well-developed biotite foliation. The biotite has a light to medium brown color and often multiple dark brown to black radioactive haloes from zircon or monazite inclusions can be observed. The crystals can attain thicknesses of up to 300 μm and can have a strongly developed poikiloblastic texture, often in association with intensely sericitized feldspar. The feldspar crystals show sericitization especially along cleavage/twin planes. Intense tourmalinization also often occurs. The tourmaline crystals show a poikiloblastic texture, a blue to green-brown color, sometimes zoned and have a very large size range: from a few tens of μm to 1.5 mm. Associated with tourmaline and pyrite, chlorite occurs, typically with a very pale green color. Chloritization of biotite was observed in the mafic bodies, as well as occasional white mica crystallization and silicification.

3.5. Interpretation and parageneses

The parageneses in Fig. 5 summarize the petrographical observations, subdivided according to the region and host rock composition (metasediment or mafic intrusive). These parageneses are discussed below, generalized for the whole study area. Contact metamorphic effects are local and have not been included in the regional parageneses of Fig. 5 but are discussed separately.

3.5.1. Regional metamorphism

Regionally occurring metamorphic minerals in the metasediments can be subdivided according to their relation with the bedding-parallel S_{f1} and oblique, axial planar S_{f2} foliations (Fig. 5). The occasional albite nodules and biotite porphyroblasts were observed to deflect bedding-parallel S_{f1} foliation and hence represent early-metamorphic blasts (Fig. 4d). Graphite, interpreted to have its origin in sedimentary carbonaceous material (cf. Klein and Dutrow, 2007), belongs to the pre-to syn-foliation assemblage as well. Together with white mica, biotite, medium green chlorite and in some cases elongated small quartz crystals, graphite defines both the bedding-parallel and oblique metasediment foliations (Fig. 4b, 4m and 4°).

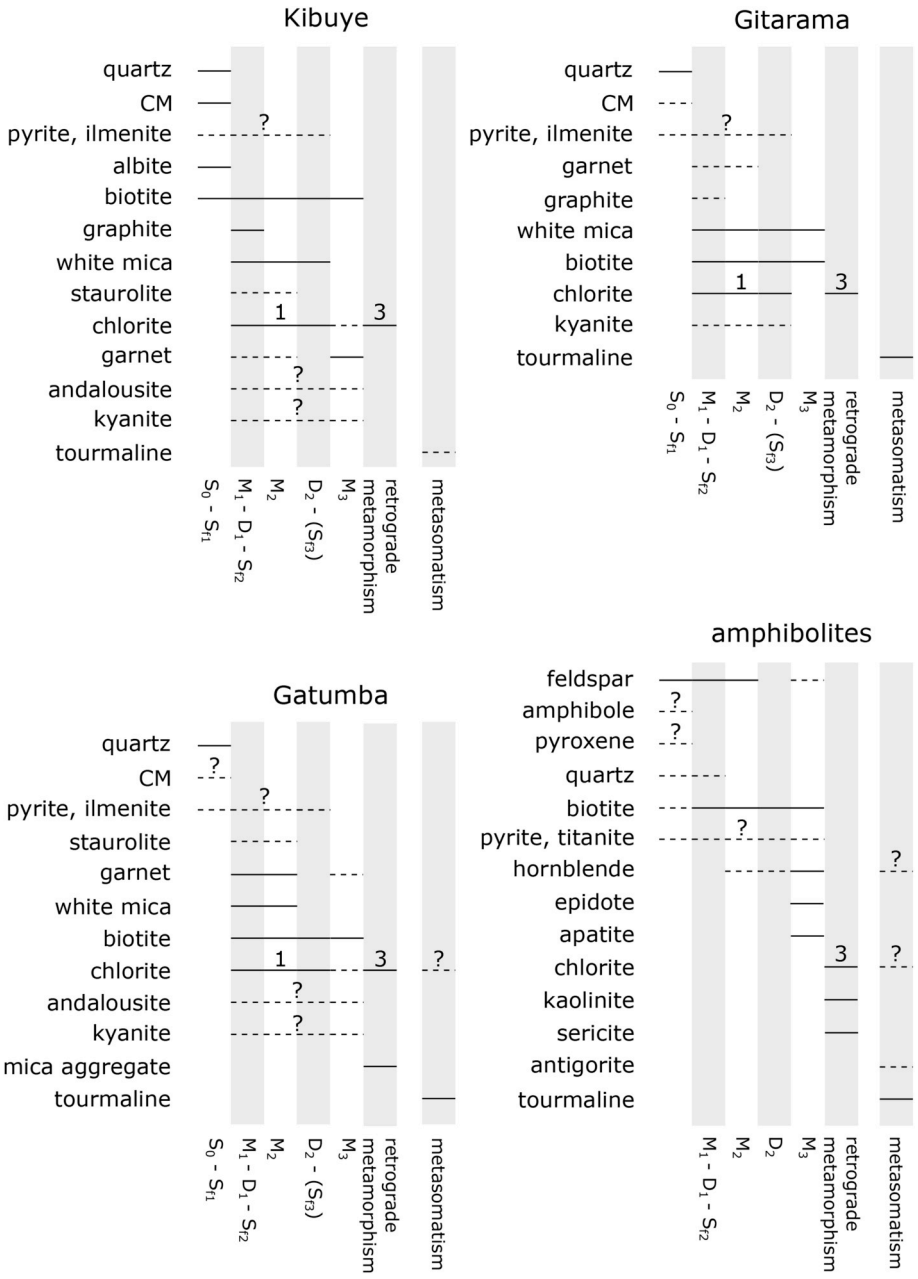

Fig. 5. Parageneses for the Kibuye, Gitarama and Gatumba metasediments and amphibolites. CM = carbonaceous material. Three chlorite types were distinguished: type 1 = regional metamorphic chlorite, Fig. 4j, type 2 (not included in these regional parageneses) = contact metamorphic chlorite, Fig. 4c, and type 3 = retrograde chlorite, Fig. 4k. Note that based on petrographical arguments, it is not clear at which stage metasomatism took place. Therefore it is displayed separately in these parageneses.

Staurolite porphyroblasts and white mica lenses demonstrate an S_{f2}-parallel orientation hence predate the deformational event that developed this oblique foliation (Fig. 4f and m). This deformation event is the major deformation event D1, which likely took place at the end of the Neoproterozoic (c. 1.0 Ga), just prior to the G4 granite and pegmatite intrusions, and which shaped the regional geometry of the Western Domain of the KAB during the Mesoproterozoic (Tack et al., 2010; Fernandez-Alonso et al., 2012; Hulsbosch et al., 2017). Most garnet grew before the major foliation development associated to this D1 deformation. This is evidenced from the relationship with the axial planar S_{f2} foliation (Figure 4o) and the occurrence of quartz pressure shadows. At a syn-to post-foliation stage, kyanite porphyroblasts developed, indicated by the internal foliation in kyanite from the Gitarama area (Fig. 4k). No constraints on the growth of andalusite and kyanite could be put in the Kibuye and Gatumba areas (Fig. 5).

The occurrence of a second deformational event, D2, is indicated by foliation textures around tourmaline. Abundant tourmaline crystallization in country rocks in the region is often reported and associated to metasomatism induced by emplacement of the G4 granite-pegmatite system (Hulsbosch and Muchez, 2019). However, in sample KG45, tourmaline is wrapped by the chlorite host rock foliation, which therefore is interpreted to represent the Neoproterozoic S_{f3} foliation (Fig. 4g). In addition, two oblique foliation generations (S_{f2} & S_{f3}) were occasionally observed in outcrops and samples. Nevertheless, in most samples, only one axial planar foliation (S_{f2}) was observed, suggesting D2 (during which S_{f3} developed) in most cases merely reinforced the pre-existing foliation S_{f2} that developed during D1. Euhedral, post-foliation (post-D2) garnet porphyroblasts (Fig. 4e) were only observed in Kibuye samples, in contrast to the Gitarama and Gatumba area. Together with biotite and white mica, garnet hence belongs to a younger,

post-deformational metamorphic assemblage.

Metapelitic rocks of the Kibuye-Gitarama-Gatumba area thus show a uniform Barrovian-type increase in metamorphism from prograde lower greenschist facies (graphite, chlorite, white mica, albite), over upper greenschist facies (garnet, biotite) up to lower amphibolite facies conditions (staurolite, kyanite; cf. Best, 2002). This prograde assemblage is further referred to as M1–M2 in this manuscript. The twofold prograde Barrovian metamorphic trajectory is postulated based on the two garnet generations determined with electron probe microanalysis (EPMA) element maps and Lu–Hf geochronology (one older than 920 Ma and one which formed around 880 Ma) with both pre-deformational (D2) characteristics (Van Daele & Scherer, *in revision*). It is not possible to determine the exact paragenetic position of staurolite and kyanite relative to the deformation events D1 (*c.* 1.0 Ga; Fernandez-Alonso et al., 2012) and D2 (< 880 Ma; Van Daele and Scherer, *in revision*). However, the intense foliation wrapping around staurolite (Fig. 4f) and internally present in kyanite (Fig. 4k), suggests these minerals grew at a pre- and syn-to post-D1 stage, respectively, i.e. during M1. Peak metamorphic conditions are represented by the assemblages biotite–white mica–garnet ± staurolite(–chlorite) and locally kyanite–biotite(–white mica–chlorite). At a post-D2 stage, greenschist facies conditions prevailed in the study area, as demonstrated by the post-foliation M3 garnet–white mica–biotite(–chlorite) assemblage (Fig. 5).

The metamorphic assemblage feldspar–hornblende–biotite–epidote recorded in the KGG amphibolites reflects a syn-to post-D2 timing (Fig. 4h). If present, the foliation is defined by biotite, while the hornblende crystals mostly do not show a preferred orientation. In accordance with the metapelites, post-deformation M3 greenschist to epidote-amphibolite facies conditions can be inferred from the observed mineralogical assemblage in the amphibolites (cf. Best, 2002). No mineral relicts of the pre-deformational (lower amphibolite facies) M1–M2 metamorphism seem to be preserved in these rocks.

3.5.2. Metasomatism

Metasomatism induced crystallization of tourmaline in metasediments and mafic intrusions (Figure 4m). Tourmaline occurs dispersed throughout the matrix, other porphyroblasts and the white mica pseudomorph lenses. These effects are especially intense in the Gatumba and Gitarama areas, while in the Kibuye area tourmaline is only sporadically present as very thin, dispersed needles. This indicates the close genetic link between metasomatism and the abundant granite and pegmatite intrusions in Gatumba. Epidote was observed in the amphibolites close to pegmatite intrusions. Rare antigorite (Figure 4r) indicates hydrothermal alteration of Mg-rich (ultra-)mafic rocks, as this mineral typically forms by hydration of Mg-silicates (olivine, pyroxene or amphibole) in mafic rocks (Klein and Dutrow, 2007). In most samples the dispersed character or small size of the metasomatic minerals in largely unfoliated rocks do not allow to uniquely determine the timing of metasomatism relative to regional and retrograde metamorphism. In the foliated samples, tourmaline and antigorite disturb and define the foliation, respectively, hence crystallized at a pre-deformation time. Since the pegmatites post-date D1, tourmaline and antigorite must have formed before D2, hence metasomatism occurred at a pre-D2 stage. As it concerns a local effect of varying intensity per sample, metasomatism is put separate in the parageneses (Fig. 5).

3.5.3. Retrograde metamorphism

The main influence of retrograde metamorphism in the study area is (incomplete) chloritization of biotite (Fig. 4b, 4n and 5). Sericitization and kaolinitization of feldspar in the amphibolite and pegmatite bodies was observed as well. The origin of the white mica aggregates (heterogeneous size distribution but generally fine-crystalline; Figures 4m and q) observed as pseudomorphs of pre-deformational, elongated lenses (originally probably staurolite or kyanite), is not clear. Likely, this could also be a retrograde effect (Yardley and Baltatzis, 1985).

3.5.4. Magmatism and contact metamorphism

The amphibolite dykes were emplaced at a pre-D1 stage, as indicated by the presence of an internal foliation, the deflection of the host rock foliation near the mafic bodies and its occasional boudinaged character. Diorite contact metamorphism resulted in the crystallization of colorless (i.e. Mg-rich) chlorite, hornblende and biotite in the surrounding metasediments (Figure 4r).

The two granite types observed correspond to the two granite generations observed in the KAB, i.e. the foliated, pre-D1 G1-G3 granite and coarse, unfoliated, post-D1 G4 or Sn leucogranite (cf. Tack et al., 2010). Pegmatites mainly intruded in pre-existing discontinuities created by D1, such as the bedding or S_{f2} foliation, or in mafic bodies (e.g., Hulsbosch et al., 2017). The pegmatites neither underwent intense metamorphism nor show intense deformation apart from boudinage in a few cases. Combined with the occasional occurrence of pegmatites trapped in fold hinges, this indicates a post-D1, pre-to syn-extensional emplacement (Hulsbosch et al., 2017; Butler and Torvela, 2018). White mica and quartz (re-)crystallization are typical contact metamorphic effects of felsic magmatism in the metasediments, observed to be most intense close to granitic and pegmatitic intrusions. Possibly, the large unoriented poikiloblastic biotite porphyroblasts also have a contact metamorphic origin as these are only observed in contact aureole rocks. However no conclusive arguments for this hypothesis can be drawn based on the few samples containing these features. Contact metamorphosed amphibolite bodies typically contain abundant biotite. In general, contact metamorphic effects diminish strongly at distances > 20 cm from the pegmatite or granite body increases.

3.5.5. Three chlorite types in the Kibuye-Gitarama-Gatumba area

As discussed in the paragraphs above, three types of chlorite were distinguished in the metasediments and mafic rocks in the KGG area. Dominantly, chlorite has a light to medium green color and a homogeneous clear texture (i.e. no inclusions or intergrowths of other minerals), regardless if the crystals define the foliation or are concentrated in nests or thin veins (Fig. 4a, 4l and 4m). This chlorite is interpreted as part of the prograde regional metamorphic assemblage and is further referred to as chlorite type 1. Secondly, colorless (non-pleochroic) chlorite was observed in metasediments near mafic intrusions, indicative of its contact-metamorphic origin (chlorite type 2; Fig. 4c). Lastly, impure chlorite with biotite interstratifications or relicts (chlorite type 3) was often observed throughout the study area. This biotite chloritization represents retrograde metamorphism (Fig. 4b, 4n and 5).

4. Mineral chemistry

4.1. Methodology

Mineral compositions (garnet, biotite, chlorite and feldspar) were analyzed by a JEOL Field Emission Gun Electron Probe Micro-Analyzer (FEG-EPMA) JXA-8530F at the Department of Material Engineering (MTM), KU Leuven. The measurements were carried out using five wavelength dispersive spectrometers (WDS) under the following conditions: accelerating voltage of 20 kV, beam current of 20 nA and beam diameter of 5 μm, peak position analysis time of 20 s, upper and lower background position analysis time of each 5 s. Standard reference materials of diopside (Si, Mg, Ca), albite (Al, Na), synthetic rutile (Ti), rhodonite (Mn), orthoclase (K, Al) and hematite (Fe) were used for external calibration. ZAF corrections for atomic number effects (Z), absorption (A) and fluorescence (F) were applied on all results. For each sample, three to five crystals or crystal pairs were analyzed, corresponding to 15 or more analysis points per mineral per sample. Water contents of biotite and chlorite were calculated stoechiometrically by the spreadsheets provided by Tindle (2001a, 2001b). Assuming full site occupancy, i.e. no octahedral vacancies, the Fe^{3+}-content of chlorite could be estimated using the same spreadsheet. Total oxide values of

the analyzed minerals range between 98.2 and 100.7 wt%.

4.2. Sample selection

Twenty-one representative samples were selected for quantitative mineral composition analysis with FEG-EPMA and characterization of the different metamorphic and metasomatic conditions in the Kibuye and Gatumba area (Fig. 2). Gitarama area samples were not used due to their generally weathered character. The sample collection comprises twelve metasedimentary samples (of which two contain deformed quartz-garnet-biotite veins), one hornfels, one metamafic rock and seven amphibolites. In Table 1, a summary of locality, rock type and mineralogy is given for all samples.

Table 1
Selected samples and their locality, geological and mineralogical characteristics, and applied geothermometers. Mineral abbreviations after Siivola and Schmid (2007). Cy = Cyurugeyo Formation, Sa = Sakinyaga Formation, St = Satinsyi complex, Ga = Gatwaro Formation, GB = garnet-biotite geothermometry, Chl = chlorite geothermometry, QGB = metasiltstone with quartz vein rimmed by garnet-biotite zone.

Sample	Location	Latitude (°S)	Longitude (°E)	Rock type	Group
07	Kibuye	2° 06′ 06″	29° 19′ 53″	metasandstone	Pindura (Cy)
08	Kibuye	2° 06′ 05″	29° 19′ 53″	metasiltstone	Pindura (Cy)
17–01	Gatumba	1° 55′ 20″	29° 39′ 31″	amphibolite	Cyohoha (St)
17–02	Gatumba	1° 55′ 17″	29° 39′ 15″	amphibolite	Cyohoha (St)
18	Kibuye	2° 04′ 41″	29° 22′ 24″	metasiltstone	Cyohoha (Sa)
22	Kibuye	2° 04′ 26″	29° 22′ 29″	amphibolite	Cyohoha (Ga)
27	Kibuye	2° 04′ 30″	29° 22′ 34″	hornfels	Cyohoha (Ga)
29	Kibuye	2° 04′ 51″	29° 23′ 12″	amphibolite	Cyohoha (Ga)
43	Kibuye	2° 05′ 53″	29° 20′ 13″	metasiltstone	Pindura (Cy)
52	Kibuye	2° 05′ 31″	29° 19′ 55″	amphibolite	Pindura (Cy)
53	Kibuye	2° 06′ 09″	29° 20′ 07″	amphibolite	Pindura (Cy)
91	Gatumba	1° 55′ 34″	29° 39′ 13″	metamafic	Cyohoha (St-Ga)
96	Gatumba	1° 55′ 43″	29° 39′ 02″	metasiltstone	Cyohoha (St-Ga)
97	Gatumba	1° 55′ 42″	29° 39′ 01″	metasiltstone	Cyohoha (St-Ga)
101	Gatumba	1° 55′ 42″	29° 38′ 58″	metasiltstone	Cyohoha (St-Ga)
112	Gatumba	1° 56′ 56″	29° 39′ 35″	metasiltstone	Cyohoha (St-Ga)
122	Gatumba	1° 55′ 20″	29° 39′ 28″	amphibolite	Cyohoha (St)
123	Gatumba	1° 56′ 55″	29° 39′ 21″	QGB vein	Cyohoha (St-Ga)
124	Gatumba	1° 56′ 55″	29° 39′ 20″	QGB vein	Cyohoha (St-Ga)
125	Gatumba	1° 56′ 47″	29° 39′ 16″	metasiltstone	Cyohoha (St-Ga)
130	Gatumba	1° 56′ 55″	29° 39′ 17″	metasiltstone	Cyohoha (St-Ga)

Sample	Mineralogy	geo-T
07	matrix (qtz, gr, bt, wmca) with large grt and chloritized bt porphyroblasts	Chl
08	garnet-rich metasiltstone (qtz, gr, bt, wmca)	GB
17–01	fsp (sericitized), am, minor amounts of bt, py, ep, qtz, ap, tur	
17–02	am, fsp (sericitized), bt, minor amounts of chl, ep, qtz, tur, py	
18	chlorite schist (minor amounts of am, qtz, fsp, bt, rt, tur) at contact with to diorite	Chl
22	am, fsp, qtz, minor amounts of bt, ep, py	
27	metasiltstone (qtz, bt, chl, wmca, gr, tur)	Chl
29	am, fsp (sericitized), minor amounts of bt, qtz, chl	
43	staurolite-rich metasiltstone (qtz, wmca, bt, gr, grt, tur)	GB
52	am, fsp, qtz, minor amounts of bt, py, ap	
53	am, fsp, minor amounts of qtz, bt, py, ap	
91	chloritite with atg at contact with diorite	Chl
96	qtz-rich matrix with chl, wmca, bt, fsp, grt and tm	Chl
97	metasiltstone (bt, wmca, chl, grt, tur) at contact with pegmatite	GB
101	qtz lens with bt-grt rim in gneiss (qtz, gr, bt, wmca, tur, chl)	GB
112	matrix (qtz, gr, wmca, tm) with large chlorite lenses	Chl
122	diorite (fsp, bt, chl, tur, qtz, py) at contact with pegmatite	Chl
123	quartz vein with biotite-garnet rim in metasiltstone (qtz, bt, fsp, chl, grt, tur)	GB
124	quartz vein with biotite-garnet rim in metasiltstone (qtz, bt, tur)	GB
125	metasiltstone (qtz, wmca, bt, chl, grt, tur) with large white mica aggregates	GB, Chl
130	metasiltstone (qtz, wmca, chl, bt) with large white mica aggregates	Chl

4.3. Mineral compositions

A summary of the analyzed garnet, biotite, chlorite and feldspar compositions by FEG-EPMA is presented in Table 2. Classification diagrams for garnet, biotite, feldspar and chlorite are given in Fig. 6.

4.3.1. Garnet

Table 2a and Fig. 6a show for each sample the garnet major element composition and the normalized percentages of the pyralspite group garnet endmembers (pyrope, almandine, grossular and spessartine). The andradite-content (ugrandite group) is for all samples less than 1% and is not included in the normalization. Garnets in the KGG area are typically rich in Fe, with almandine percentages varying between 65 and 81%. The spessartine-component (Mn) reaches values up to 21%, while that of grossular, the Ca-endmember, is maximum 5%. The proportion of the Mg-endmember, pyrope, varies between 6 and 10%. M1–M2 garnets (101, 123, 124 and 125) are relatively enriched in almandine ($>$ 77.5% vs $<$ 73.5%) while the M3 garnets (08 and 43) and M1–M2 garnet 97 show a slightly higher spessartine component ($>$ 14% vs $<$ 12%). The ranges of pyrope and grossular content overlap for both garnet types. Post-deformational M3 garnets show a uniform chemical zonation as expected during garnet growth (e.g. Mn decrease from core to rim; Kohn, 2003), while in some of the larger pre-deformational M1–M2 garnets, a fractured, relic core (interpreted as M1) overgrown by a younger, chemically distinct rim can (interpreted as M2) be recognized (Van Daele and Scherer, in revision).

4.3.2. Biotite

In Fig. 6b, the biotite results are plotted in the mica classification diagram of Tischendorf et al. (1997), which is based on the cations present in the octahedral position. M3 biotite from samples 08 and 43 (Kibuye) has a Mg-biotite composition. Gatumba biotite (part of the M1–M2 assemblage) shows a slightly different composition. The biotite of sample 97 is located at the boundary between Fe- and Mg-biotite, while biotite of all other Gatumba samples is classified as Fe-biotite. Except for sample 123, limited compositional variation within one sample is observed for biotite in the KGG area.

4.3.3. Feldspar

Feldspar in the amphibolites of the Kibuye and Gatumba areas typically has a plagioclase composition (Table 2c, Fig. 6c). The orthoclase component varies between 0.2 and 0.8%. However, the different feldspars show considerable variation along the plagioclase solid-solution series ($CaAl_2Si_2O_8$–$NaAlSi_3O_8$), even within one sample. Feldspar of amphibolites 17-02 and 29 shows the most internal variation with an anorthite component ranging between 45 and 65 wt%, i.e. of labradorite to andesine composition. Feldspar of samples 17-01, 52 and 53 clusters together, with an anorthite component between 30 and 40%, i.e. belonging to the andesine-type. Samples 17 and 22 show the least compositional variation and contain the most albitic feldspar (72 and 78% respectively), classifying as oligoclase. As the amphibolites are largely unfoliated, it is not possible to petrographically distinguish the M1–M2 assemblage minerals from the M3 assemblage minerals.

4.3.4. Chlorite

The major element composition of chlorite within each sample is rather homogeneous. The implementation of the chlorite samples in the classification scheme of Hey (1954) is shown in Fig. 6d. The #Fe-value [$Fe_{tot}/(Fe_{tot}+Mg)$] is approximately constant for each sample, as well as the amount of Si (apfu), except for samples 91 and 125. The most Fe-rich (and consequently Mg-poor) chlorite was observed in sample 125. This sample, as well as chlorites 07, 96, 122 and 130, all part of the post-deformational M3 assemblage, belongs to the ripidolite variety. A similar composition is found for chlorite of sample 112, where chlorite is part of the M1–M2 assemblage. Chlorite of samples 18 (contact metamorphic chlorite) and 27 (M1–M2 assemblage) is categorized as

Table 2
FEG-EPMA mineral composition data of the Kibuye-Gatumba samples. (**a**) garnet, (**b**) biotite, (**c**) feldspar and (**d**) chlorite. The data represents the average (av) and two standard deviation value (2 sd) of all mineral analyses of one particular sample. All values are in wt%, except for the garnet and feldspar normalizations (%). * = calculated stoechiometrically according to Tindle (2001a, b).

Garnet

	08 *(n = 15)*		43 *(n = 15)*		97 *(n = 15)*		101 *(n = 15)*		123 *(n = 15)*		124 *(n = 15)*		125 *(n = 15)*	
	av	2 sd	av	2 sd	av	2 sd	av	2 sd	av	2 sd	av	2 sd	av	2 sd
SiO_2	36.97	0.33	37.51	0.89	37.43	0.39	36.89	0.56	36.62	0.27	37.18	0.18	37.20	0.17
Al_2O_3	21.15	0.22	20.63	0.27	20.47	0.17	20.36	0.29	21.02	0.16	20.41	0.10	20.59	0.25
FeO^T	30.03	0.43	32.44	0.35	29.93	0.21	35.16	0.38	33.78	0.52	34.92	0.64	35.66	0.42
MnO	7.04	0.24	6.15	0.17	8.88	0.20	3.95	0.17	5.31	0.50	3.50	0.44	3.39	0.46
MgO	2.43	0.10	2.53	0.14	1.77	0.03	1.81	0.07	1.64	0.10	1.89	0.02	1.69	0.01
CaO	1.78	0.08	0.67	0.01	1.21	0.09	1.18	0.04	1.21	0.25	1.69	0.08	1.47	0.11
Total	99.40		99.93		99.69		99.35		99.58		99.59		100.00	
Almandine	68.81		73.42		68.33		79.82		77.49		79.04		80.87	
Spessartine	16.18		14.28		20.78		9.24		12.28		8.18		7.87	
Pyrope	9.84		10.34		7.31		7.45		6.69		7.79		6.92	
Grossular	5.17		1.96		3.58		2.88		3.53		4.53		4.22	

Biotite

	08 *(n = 14)*		43 *(n = 15)*		97 *(n = 15)*		101 *(n = 15)*		123 *(n = 14)*		124 *(n = 15)*		125 *(n = 14)*	
	av	2 sd	av	2 sd	av	2 sd	av	2 sd	av	2 sd	av	2 sd	av	2 sd
SiO_2	37.11	0.96	36.26	0.87	35.52	0.71	35.13	0.54	34.59	1.51	34.75	0.75	34.91	0.68
TiO_2	1.38	0.11	1.46	0.32	1.65	0.13	1.40	0.09	1.43	0.07	1.40	0.07	1.39	0.01
Al_2O_3	19.25	0.26	19.44	0.59	17.86	0.12	18.83	0.43	19.01	0.98	18.89	0.73	19.05	0.46
FeO^T	18.12	0.68	18.01	0.36	20.82	0.45	21.82	0.25	26.37	2.20	22.38	2.62	22.26	1.07
MnO	0.02	0.02	0.087	0.013	0.17	0.03	0.051	0.016	0.15	0.002	0.15	0.05	0.06	0.01
MgO	10.93	0.19	9.87	0.69	9.20	0.21	8.32	0.26	6.87	0.63	8.02	1.01	7.81	0.15
K_2O	8.67	0.55	9.68	0.09	9.75	0.10	8.95	0.51	8.33	1.34	8.80	0.40	9.28	0.30
H_2O*	4.08	0.07	3.96	0.05	3.89	0.04	3.87	0.04	3.91	0.11	3.85	0.06	3.87	0.03
Total	99.55		98.77		98.86		98.38		100.66		98.24		98.62	

Chlorite

sample	07 *(n = 15)*		18 *(n = 15)*		27 *(n = 14)*		91 *(n = 15)*		96 *(n = 18)*		112 *(n = 15)*		122 *(n = 19)*		125 *(n = 14)*		130 *(n = 15)*	
type	type 3		type 2		type 1		type 1/3?		type 3		type 1		type 3		type 3		type 1 (3)	
	av	2 sd	av	2 sd	av	2 sd	av	2 sd	av	2 sd	av	2 sd	av	2 sd	av	2 sd	av	2 sd
SiO_2	24.58	0.75	28.36	0.67	27.78	0.75	31.64	1.54	26.24	0.82	25.55	0.58	26.44	0.21	24.27	1.39	23.94	0.68
TiO_2	0.08	0.05	0.05	0.03	0.07	0.04	0.06	0.05	0.08	0.03	0.07	0.03	0.04	0.02	0.10	0.10	0.09	0.05
Al_2O_3	23.66	0.39	22.30	1.08	24.17	0.79	17.84	2.48	22.65	1.14	22.91	0.94	21.31	0.20	23.10	1.41	23.04	0.41
Fe_2O_3*	0.59	0.50	0.48	0.26	1.01	0.38	n.a.	n.a.	0.98	0.63	0.39	0.30	0.41	0.36	0.82	0.50	0.41	0.38
FeO	22.83	0.38	10.45	0.43	10.34	0.52	5.31	1.01	18.83	1.04	21.85	0.84	20.85	0.86	28.14	0.60	27.41	0.59
MnO	0.16	0.02	0.10	0.02	0.06	0.02	0.01	0.01	0.36	0.04	0.11	0.02	0.24	0.03	0.08	0.02	0.24	0.04
MgO	15.10	0.21	25.91	0.53	24.48	0.62	32.56	1.08	17.81	0.97	17.02	0.69	17.95	0.13	11.18	0.35	12.06	0.35
H_2O*	11.42	0.17	12.34	0.07	12.37	0.10	12.67	0.13	11.65	0.08	11.63	0.10	11.60	0.08	11.19	0.08	11.16	0.08
Total	98.42		100.00		100.28		100.09		98.60		99.53		98.84		98.88		98.35	

Feldspar

	17-01 *(n = 15)*		17-02 *(n = 15)*		22 *(n = 13)*		29 *(n = 16)*		52 *(n = 15)*		53 *(n = 15)*	
	av	2 sd	av	2 sd	av	2 sd	av	2 sd	av	2 sd	av	2 sd
SiO_2	58.77	0.54	52.68	5.33	61.86	1.01	53.57	3.64	58.86	1.79	59.12	0.76
Al_2O_3	25.83	0.21	29.63	3.86	23.35	0.94	28.84	2.33	25.75	1.42	25.70	0.40
FeO^T	0.062	0.02	0.081	0.03	0.180	0.11	0.45	0.24	0.062	0.03	0.070	0.10
CaO	7.24	0.27	11.58	4.31	4.64	0.22	10.94	2.73	7.07	1.52	6.95	0.53
Na_2O	7.61	0.12	5.02	2.58	9.20	0.13	5.31	1.62	7.85	0.91	7.88	0.39
K_2O	0.078	0.03	0.073	0.06	0.050	0.05	0.13	0.05	0.037	0.01	0.053	0.02
Total	99.59		99.07		99.28		99.24		99.64		99.77	
Anorthite	34.29	1.42	55.92	10.60	21.70	2.05	52.47	6.99	33.18	4.99	32.70	1.43
Albite	65.27	1.44	43.66	10.61	78.05	2.02	46.79	7.14	66.62	5.03	67.00	1.40
Orthoclase	0.44	0.09	0.42	0.36	0.25	0.22	0.74	0.37	0.21	0.04	0.29	0.22

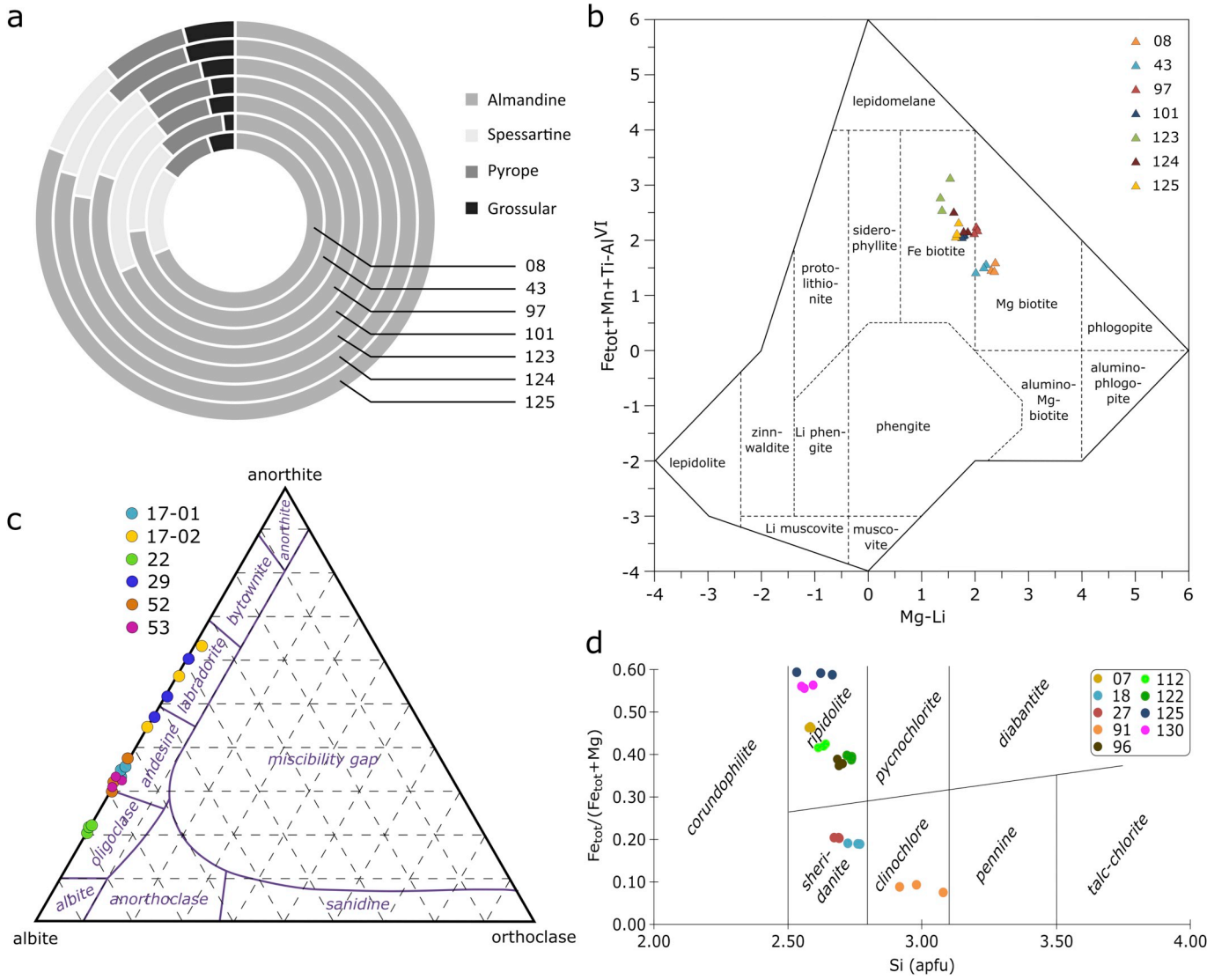

Fig. 6. Mineral classification with implementation of the Kibuye-Gatumba samples. (**a**) Garnet endmember proportions. (**b**) Mica classification of Tischendorf et al. (1997). (**c**) Triangular feldspar diagram. (**d**) Chlorite classification of Hey (1954).

sheridanite, the corresponding Mg-enriched type. Chlorite of sample 91 (contact metamorphic chlorite) contains more Si and is classified as clinochlore. Hence, chlorite composition is not exclusively related to the metamorphic assemblage it belongs to.

5. Geothermometry

Given the extensive metasomatism, a closed system cannot be assumed and classic pseudosection modeling to reconstruct the P-T path is not possible. Therefore, bulk-rock independent geothermometric methods which rely on individual and inter-mineral equilibria are applied on the samples of the KGG area.

5.1. Garnet–biotite geothermometer

Many empirical and thermodynamic garnet–biotite geothermometers have been proposed in literature. Based on the applied experimental settings, geological context (P, T, mineral assemblage), geochemical boundary conditions (e.g. maximum Ti-content in biotite) and solid solution mixing models of garnet and biotite, the method proposed by Hoinkes (1986) is considered to be most applicable for the samples of this study. The Ti- and Al^{VI}-contents of KGG biotite fall within the ranges observed in the biotite analyzed by Hoinkes (1986). Hence, the extent to which these substitutions could have influenced the Fe–Mg exchange is small and ideal mixing between the biotite solid solutions can be justified (Hoinkes, 1986). An additional reason why the model of Hoinkes (1986) was chosen, is that it has proven to give good results for greenschist and amphibolite facies rocks with a similar mineralogy as the Kibuye-Gatumba samples. Hoinkes (1986) corrects the experimentally calibrated Ferry and Spear (1978) formula for the effect of Ca in garnet on the partitioning of Mg and Fe between garnet and biotite. Based on regression of natural samples from the southern Ötztal, Austria, Hoinkes (1986) provides an empirical temperature equation including a correction term with X_{Ca}^{grt}:

$$T\,(°C) = \frac{2089 + 0.00956 \times P(bar)}{0.7821 - \ln K_D - 2.978 \times X_{Ca}^{grt} + 5.906 \times (X_{Ca}^{grt})^2} - 273$$

The reference pressure, necessary to carry out the calculations, was set at 5 kbar, in accordance to pressure ranges proposed for peak metamorphism in the Kivu area and NW Burundi based on the metamorphic minerals observed and geothermobarometric calculations (Nahimana, 1988; Rumvegeri, 1991) and the similar maximum pressures obtained for the early Neoproterozoic G4 granite and pegmatite intrusions in the Gitarama-Gatumba area based on the occurrence of

Table 3
Garnet-biotite temperature calculations for the Kibuye-Gatumba samples according to the model of Hoinkes (1986). Kib = Kibuye, Gat = Gatumba, meta = metasiltstone, QGB = quartz-garnet-biotite vein.

Crystal	$\frac{XMg^{grt}}{XFe}$	$\frac{XMg^{bt}}{XFe}$	K_D	$X_{Ca}{}^{grt}$	Calculated temperature	Average temperature per sample	
08A	0.145	1.060	7.31	0.050	537 °C	08	
08B	0.143	1.070	7.50	0.051	530 °C	meta	529 ± 7 °C
08C	0.142	1.097	7.75	0.052	521 °C	Kib	
43B	0.088	0.468	7.13	0.019	521 °C	43	
43C	0.086	0.457	7.10	0.019	522 °C	meta	525 ± 5 °C
43D	0.084	0.476	6.89	0.020	532 °C	Kib	
97A	0.140	0.995	7.62	0.035	513 °C	97	
97B	0.134	0.949	7.29	0.037	528 °C	meta	520 ± 6 °C
97C	0.143	0.987	7.53	0.035	517 °C	Gat	
101A	0.105	0.799	7.49	0.034	518 °C	101	
101B	0.107	0.779	7.27	0.035	528 °C	meta	523 ± 4 °C
101C	0.104	0.785	7.38	0.034	523 °C	Gat	
123A	0.091	0.679	5.29	0.035	635 °C	123	
123B	0.094	0.687	5.29	0.033	634 °C	QGB	627 ± 11 °C
123C	0.091	0.674	5.68	0.038	612 °C	Gat	
124A	0.097	0.555	5.71	0.048	619 °C	124	
124B	0.097	0.687	7.05	0.050	549 °C	QGB	571 ± 34 °C
124C	0.097	0.684	7.09	0.050	547 °C	Gat	
125A	0.084	0.626	7.42	0.042	527 °C	125	
125B	0.085	0.635	7.48	0.045	527 °C	meta	529 ± 2 °C
125C	0.084	0.616	7.30	0.042	532 °C	Gat	

andalusite and spodumene, and on fluid inclusion research (Pohl et al., 2013; Lehmann et al., 2014; Hulsbosch and Muchez, 2019). When the pressure is changed with 1 kbar, temperature calculations only give differences of *c.* 4 °C, limiting the importance of pressure on the temperature calculations. The K_D value was calculated assuming ideal mixing: $\left(\frac{Mg}{Fe}\right)^{bt}/\left(\frac{Mg}{Fe}\right)^{grt}$. The Ca-content of garnet is calculated as $X_{Ca}^{grt} = \frac{Ca}{Mg + Fe + Ca + Mn}$. The results of these calculations are given in Table 3.

Two samples of the Kibuye area were analyzed for garnet-biotite geothermometry. Sample 08 is a grey quartz–graphite–biotite–white mica(–pyrite–tourmaline) metasiltstone with extremely euhedral post-D2, M3 garnet porphyroblasts (up to 2 vol%) that occur dispersed in the matrix (Fig. 4e). In contrast, sample 43 is a quartz–white mica–biotite–graphite(–pyrite–tourmaline) metasiltstone which contains abundant cm-sized, pre-deformational M1–M2 staurolite crystals (Figs. 3a–4f) and only a minor amount of small euhedral and post-deformational M3 garnet and biotite porphyroblasts. Although the two samples from the Kibuye-Cyangugu transect, i.e. 08 and 43, each represent a different mineral assemblage frequently observed in metasediments of the Cyurugeyo Formation, they both give within error identical garnet–biotite temperatures, i.e. 529 ± 7 and 525 ± 5 °C.

The five sub-to anhedral garnets of the Gatumba area (KG97, 101, 123, 124 and 125) represent the pre-D2 M1–M2 assemblage. Such garnets were also observed occasionally in the Kibuye samples, however, their altered condition does not allow to determine their composition. According to their garnet–biotite temperature and lithology, the Gatumba samples can be subdivided into two groups. Sample 97 was collected in the Gatumba-Kirengo transect from a metasiltstone next to a 5 cm thick quartz-rich veinlet, possibly pegmatitic in origin. Garnets in this sample are surrounded by mostly randomly oriented biotite crystals. Sample 101, also from the Gatumba-Kirengo river section, represents the garnet–biotite zones often observed in gneissic metasiltstone close to foliation-parallel elliptical quartz pockets (Fig. 3k). Garnet in this sample shows similar characteristics as sample 97. Sample 125 was collected in the southern Malirakabibi-Magunda river transect. In this sample, disperse subhedral garnet and biotite crystals are present in a quartz–white mica–chlorite matrix which contains large white mica aggregates, possibly originally staurolite as in sample 43 (Figures 4o and q). The phyllosilicate foliation clearly shows that the garnets grew during a pre-deformational stage. These three metasiltstone samples (97, 101 and 125) show garnet–biotite temperatures similar to those of the Kibuye area: 520 ± 6, 523 ± 4 and 529 ± 2 °C, respectively. The other two samples, 123 and 124, are closely located to sample 125 (Fig. 2) and were sampled from quartz veins (± 3 cm thick) with a garnet–biotite rim up to 1 cm thick. In sample 124, the garnet(–biotite) rim is entirely included in the quartz vein, while in sample 123, the garnet-enriched zone partially is present both in the host rock as well as in the quartz vein. The garnet–biotite temperatures of these two samples are significantly higher than the rest of the samples: 627 ± 11 and 571 ± 34 °C respectively.

5.2. Chlorite geothermometry

The model of Vidal et al. (2001) was selected as the most suitable for chlorite geothermometry of the quartz-bearing Kibuye-Gatumba rock samples. It is amongst the most elaborate models for Fe–Mg aluminous chlorite geothermometry (Si < 3 apfu) and gives valid results for metapelites over a large range of temperature and pressure conditions (Vidal et al., 2001). More specifically, it is the only model that can be used for chlorite which formed at a temperature higher than 500 °C, hence ideal for metamorphic chlorite. Three equilibrium reactions are considered with the endmembers clinochlore [$Mg_5Al_2Si_3O_{10}(OH)_8$], daphnite [$Fe_5Al_2Si_3O_{10}(OH)_8$], amesite [$(Fe,Mg)_4Al_4Si_2O_{10}(OH)_8$] and sudoite [$(Fe,Mg)_2Al_4Si_3O_{10}(OH)_8$], accounting for Tschermak, di- and trioctahedral substitution. The three K_{eq}-values of these reactions allow the calculation of three equilibrium temperatures resulting in an average temperature that accounts for these substitution mechanisms. Calibration of the thermodynamic constants was done by the use of both experimental and natural chlorite data (Vidal et al., 2001). Some

Table 4
Chlorite temperature calculations (according to Vidal et al., 2001). Type 1 = regional metamorphic chlorite, type 2 = contact metamorphic chlorite, type 3 = retrograde metamorphic chlorite (detailed descriptions in text). Kib = Kibuye, Gat = Gatumba.

Sample	Reference pressure	Calculated temperature (°C)	Average temperature per sample	
07A		594 ± 61	07	
07B	3000 kbar	624 ± 75	type 3	
07D		598 ± 66	Kib	
18A		511 ± 17	18	
18B	5000 kbar	519 ± 15	type 2	
18C		605 ± 19	Kib	
27A		480 ± 2	27	
27B	5000 kbar	540 ± 10	type 1	
27C		599 ± 34	Kib	
96A		465 ± 3	96	
96B	3000 kbar	442 ± 8	type 3	459 ± 12 °C
96C		471 ± 5	Gat	
112A		655 ± 55	112	
112B	5000 kbar	605 ± 50	type 1	
112C		603 ± 50	Gat	
122A		437 ± 11		
122B		443 ± 8	122	
112C	3000 kbar	388 ± 16	type 3	437 ± 26 °C
122D		450 ± 8	Gat	
122E		466 ± 1		
125D		623 ± 81	125	
125E	3000 kbar	461 ± 15	type 3	
125F		389 ± 1	Gat	
130A		666 ± 59	130	
130B	5000 kbar	665 ± 60	type 1(3)	
130C		507 ± 27	Gat	

of these parameters, especially for Fe-amesite, were further refined by Parra et al. (2005) and Vidal et al. (2005). As for the garnet–biotite geothermometry, a pressure of 5 kbar was assumed for the regional and contact metamorphic chlorite samples (type 1 and 2). For retrograde chlorite (type 3), the pressure was arbitrarily set at 3 kbar. The effect of pressure on the temperature calculation is again limited since a pressure variation of 1 kbar corresponds to a maximum temperature variation of around 15 °C. The calculated chlorite temperatures are given in Table 4.

The chlorite temperatures show significantly more intra-sample variation than the garnet–biotite temperatures. Additionally, standard deviation values up to 75 °C (3rd column in Table 4) reflect a large variability in the temperatures obtained for each of the three geothermometers used by Vidal et al. (2001). This indicates the chlorite composition is not for all samples in full equilibrium, i.e. does not represent a single moment nor temperature or depends on local variations in host rock composition, even on the scale of a thin section. Furthermore, the model of Vidal et al. (2001) is calibrated for a temperature range of 100–600 °C. Chlorites 07B, 18C, 112, 125A, 130A and 130B exceed the upper temperature limit, suggesting that these chlorite crystals do not fulfill the compositional conditions of the model, implying a decreased reliability of the results. Average values are therefore only calculated and geologically significant for samples 96 and 122, for which temperature variability amongst the three geothermometers is limited (< 16 °C, mostly < 8 °C; Table 4).

Three type 1 chlorites were analyzed, i.e. in samples 27, 112 and 130. In the last sample, also retrograde chlorite (type 3) was observed, but crystals showing biotite relicts were avoided for the FEG-EPMA analyses. The type 1 samples represents both types of regional metamorphic M1–M2 chlorite observed in the area: i.e. foliation-parallel chlorite and chlorite nests. Sample 27 was sampled near Kibuye, in the western part of the Kibuye-Mukura transect and is a foliated quartz–white mica–biotite–graphite metasiltstone in which chlorite abundantly occurs in nests (as does biotite) and in folded veinlets of < 1 mm thick (Fig. 4a). In sample 112 (eastern end of the Magunda-Malirakabibi river transect), chlorite is present as euhedral, randomly oriented crystals concentrated in elongated lenses in a quartz–-graphite–white mica matrix (Figure 4l). Lastly, sample 130 is a metasiltstone with a white mica–chlorite foliation, some larger biotite porphyroblasts and white mica lenses (Figure 4m) from the southwestern end of the same river section. All M1–M2 chlorite generally gives variable and high temperatures, often exceeding the validity range of the model (480–666 °C).

A similar temperature range (511–605 °C) is obtained for the type 2 chlorite of sample 18, which is a hornfels collected from the contact zone between a diorite intrusion and the surrounding host rock in the western part of the Kibuye-Mukura transect. Next to type 2 chlorite as dominant mineral (> 80%), minor proportions of quartz, feldspar and euhedral amphibole porphyroblasts are present (Fig. 4c).

The composition of retrograde chlorite (type 3) was analyzed in samples 07, 96, 122 and 125. In these samples, chlorite is present both dispersed in the matrix and as clusters, with varying degrees of biotite intergrowth (which have been carefully avoided during the FEG-EPMA analyses). Sample 07 contains large, poikiloblastic chloritized biotite (up to 500 μm) in a fine-crystalline quartz–graphite–white mica–biotite matrix with occasional euhedral garnet porphyroblasts (Fig. 4b). It is located at the southern end of the Kibuye-Cyangugu transect, close to sample 08. Sample 96 is a finely laminated metasiltstone from the river transect Gatumba-Kirengo, consisting mainly of quartz, white mica, chlorite and biotite. The latter is often, at least partially, chloritized. Garnet and tourmaline occur as accessory minerals. Sample 122 was collected from an amphibolitized mafic intrusion at the boundary with a pegmatitic body near Buranga (just north of the Gatumba village), and is rich in the metasomatic mineral tourmaline. Chlorite in this sample shows a relatively homogeneous composition, and contains only occasionally biotite relicts. Sample 125 was taken along the Malirakabibi river transect, south of the Gatumba concession. This metasiltstone consists of a quartz–white mica matrix with larger biotite and chlorite crystals, dispersed subhedral garnet porphyroblasts and white mica aggregates (Figures 4o and q). In general, this sample is very similar to sample 130, except for the more pronounced biotite chloritization. Two of these type 3 chlorites allowed to calculate a well-constrained temperature of 459 ± 12 °C (sample 96) and 437 ± 26 °C (sample 112) for retrograde chlorite crystallization. The two other samples show more variation. Temperature values for sample 07 vary between 594 and 624 °C. For sample 125, chlorite shows an extremely large temperature range from 389 to 623 °C, in contrast to the garnet–biotite temperature obtained for this sample (529 ± 2 °C).

Sample 91 is situated at the northeastern end of the Gisuma river just north of the Gatumba concession and represents a Mg-rich (ultra-) mafic rock which was affected by hydrothermal alteration. Similar to sample 18 from the Kibuye area, this rocks consists dominantly of almost colorless, non-pleochroic chlorite (> 90%), but of more Fe-depleted, clinochlore composition (Fig. 6d). In addition, a minor amount of poikiloblastic, hydrothermal, partially chloritized, antigorite is present, indicating the chlorite in this sample is of post-metasomatic timing (Figure 4r). A distinction between regional or retrograde metamorphism origin could not be made based on petrography. The model of Vidal et al. (2001) and by extension all thermodynamic chlorite geothermometry models (e.g. Bourdelle et al., 2013; Lanari et al., 2014) are only valid for quartz-bearing assemblages, hence not applicable for sample 91. Additionally, this chlorite does not fulfill the chemical conditions set by the well-known empiric calibrations (Cathelineau, 1988; Hillier and Velde, 1991; Jowett, 1991). Therefore no valid temperature could be assigned to this sample.

6. Discussion

6.1. Magmatism and contact metamorphism

Granite and pegmatite contact metamorphosed rocks are characterized by quartz, white mica and biotite recrystallization. Andalusite was observed occasionally, both in the Kibuye and Gatumba areas. Unfortunately, this mineral assemblage does not allow geothermometric calculations. The presence of andalusite indicates pressure values of maximum 4 kbar during the granite intrusions. This is in accordance with Pohl et al. (2013; G1-G3 granite intrusion depth of 4–5 kbar) and Lehmann et al. (2014; G4-granite intrusion depth of 2.5–4 kbar). Dehandschutter et al. (1988), Gérards (1965) and Rumvegeri (1991) attributed their observations of staurolite, garnet, chlorite and kyanite to felsic contact metamorphism. However these minerals have been observed in the Gatumba and Gitarama area, as well as in the Kibuye area where no large granite intrusions crop out. Therefore, these minerals indicate the regional metamorphism rather than an elevated temperature regime due to contact metamorphism. Also cordierite and sillimanite are locally reported minerals attributed to contact metamorphism in the Gatumba area (Gérards, 1965; Rumvegeri, 1991), but these minerals were not observed during this petrographic study.

Temperature calculations for type 2 chlorite (diorite contact metamorphism chlorite) in the Kibuye area fall within the regional metamorphism temperature range obtained by garnet–biotite and chlorite geothermometry (Table 4, sample 18), despite the clear difference in chlorite origin and its significant Mg-enriched composition. Given the frequent foliation and amphibolitization observed in the mafic sills and dykes, which indicates a pre-deformational and pre-metamorphism intrusion timing, this contact metamorphic chlorite may have been partially re-equilibrated to regional or retrograde metamorphic conditions at a later stage. As for type 1 chlorites (§6.3), non-equilibrium conditions could explain the large temperature ranges observed for sample 18. In summary, contact metamorphism caused by both diorite and granitic/pegmatitic intrusions was chemically largely overprinted by younger metamorphism.

6.2. Metasomatism

Intense metasomatism affected the metasediments and amphibolites around the Gitarama-Gatumba granite-pegmatite complex. The main mineralogical effect of these circulating fluids is tourmalinization (Figure 4p), corresponding with the observations of Börker and Pupp (2014). Unfortunately, tourmaline does not allow geothermometric calculations. The presence of antigorite, the high-T polytype of serpentine, in meta-mafic rocks allows to broadly constrain the temperature between 250 and 600 °C (Evans, 2004). Minimal temperatures for hydrothermal alteration of 175–350 °C were inferred by fluid inclusion studies (Prochaska et al., 1992). These authors mention that the distinction between a granitic or retrograde metamorphic origin of the hydrothermal fluids could not be made. However, tourmaline in foliated rocks indicates a pre-D2 timing (Fig. 4g), which would not be in accordance with a retrograde origin. Additionally, the predominance of metasomatism in the Gitarama-Gatumba area compared to the Kibuye area and the relatively high temperature inferred from the observed antigorite suggest a genetic link with the granites.

6.3. Regional metamorphism

The most abundant regional metamorphic minerals observed in the KGG area are white mica, biotite, chlorite and garnet, in the pre-deformational M1–M2 as well as the post-deformational M3 assemblages. Large staurolite, and smaller kyanite crystals were occasionally found as part of the prograde M1 (or M2) assemblage. These minerals are in accordance with previous observations in the Western Domain of the KAB (e.g. Deblond et al., 2001; Nahimana, 1988; Rumvegeri, 1991; Tack et al., 2010), as well as in the KIB (Kokonyangi et al., 2001, 2004, 2005), confirming the representativeness and reliability of the results of the KGG study area. However, most porphyroblasts, except kyanite, do not show a syn-kinematic growth timing as described by Nahimana (1988) (Fig. 5). Rather, three different metamorphic assemblages could be identified in the metapelites: pre-to syn-deformational biotite–white mica–garnet ± staurolite(–chlorite),syn-to post-deformational kyanite–biotite(–white mica–chlorite) (M1–M2) and post-deformational garnet–white mica–biotite(–chlorite) (M3). Only one metamorphic assemblage could be recognized in the amphibolites: i.e. feldspar–hornblende–biotite(–epidote?), which represents a syn-to post-deformational timing (M3).

Previous studies, based on petrography, estimated the peak metamorphic conditions in the WD to be 520–600 °C and 4–4.8 kbar (Nahimana, 1988) and 350–800 °C, 4–8 kbar (Rumvegeri, 1991). The temperatures obtained in this study fall within these broad ranges, but are now much better constrained by the application of different independent quantitative geothermometric methods. Garnet–biotite pairs of all metasiltstones show a uniform temperature in the range of 520–529 °C (Table 3), corresponding to upper greenschist facies conditions. This is the case for the Kibuye, as well as the Gatumba area (Satinsyi complex), independent on the exact geological context and mineral or host rock composition. It is remarkable that no temperature difference was observed between the Gatumba and Kibuye areas, i.e. between pre- or post-D2 garnets respectively.

The metamorphic assemblage containing staurolite and kyanite (M1–M2), as well as the oligoclase–andesine composition of feldspar in the amphibolites (Fig. 5, Table 2c, Fig. 6c), indicates that lower amphibolite facies conditions have been reached before the post-deformational M3 greenschist conditions (Best, 2002). The significantly higher temperatures (up to 635 °C) obtained for the two samples of quartz veins with a biotite–garnet rim in the Gatumba area (123 and 124) probably represents relicts of this former metamorphic episode, preserved only in chemically relatively closed quartz vein environments. Biotite shows a larger compositional variability for these samples, especially KG124 (Fig. 6b), which is directly linked to the variability in temperature calculations. Sample 97, which has a similar geological context as samples 123 and 124, shows complete resetting towards the post-deformation greenschist facies M3 metamorphism (i.e. the regionally observed Mg-biotite composition and garnet-biotite temperature of *c.* 525 °C). These observations suggest geochemical re-equilibration of major elements between biotite and garnet towards the lower regional temperature attained during the post-D2 metamorphic M3 regime.

Chlorite thermometry is a less straightforward and robust method compared to garnet–biotite thermometry as the composition of chlorite, especially low-temperature chlorite, generally strongly depends on the host rock composition (Zane et al., 1998; Vidal et al., 2001; Lanari et al., 2012). Additionally, multiple substitution mechanisms play a role in chlorite, which are up-to-date not fully characterized. Hence thermodynamic-based models are forced to simplify the chlorite structure and substitution mechanisms. All chlorite type 1 (M1–M2) samples analyzed in this study, show a temperature range to broad to be realistic on thin section scale, and/or temperatures exceeding the thermodynamic model boundaries. The large intra-sample variation in calculated temperatures (Table 4) could be due to the presence of multiple chlorite generations in one sample, as chlorite is ubiquitous during the entire metamorphic evolution in the KGG area (Fig. 5). This can explain the lack of equilibrium amongst different chlorite crystals in one thin section. Chlorite formed during the prograde part of the regional metamorphism (M1–M2) can have been partially re-equilibrated during later conditions (e.g. contact or retrograde metamorphism).

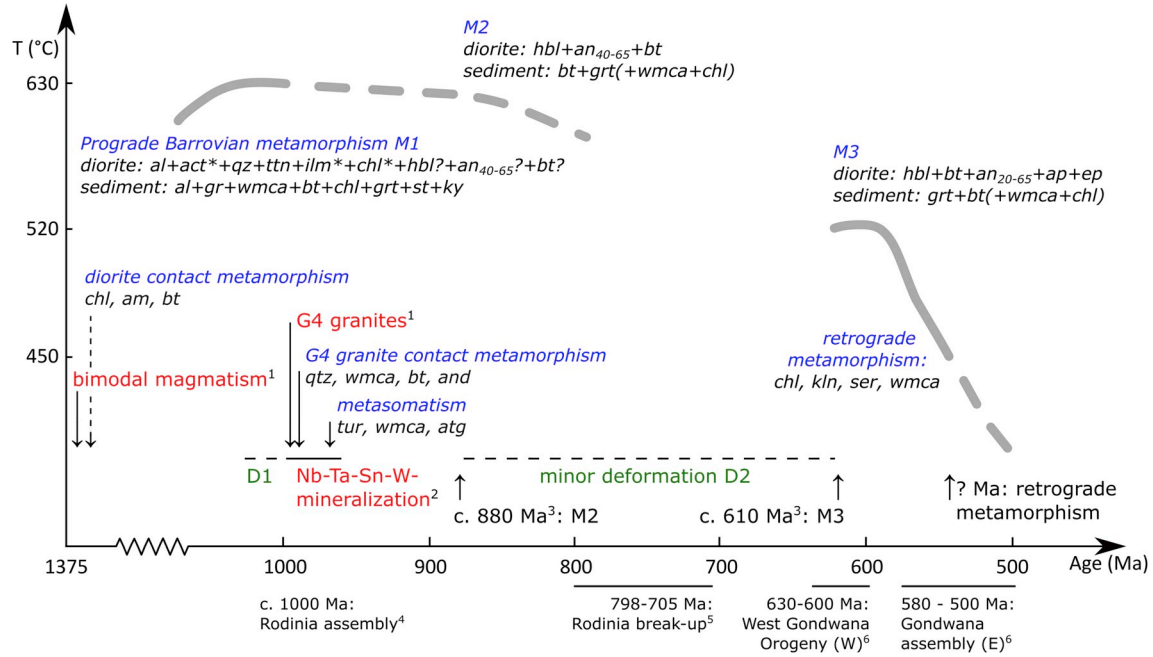

Fig. 7. Temperature evolution in the Kibuye-Gitarama-Gatumba area. Mineral abbreviations after Siivola and Schmid (2007). Green represent greenschist facies metamorphism, red amphibolite facies metamorphism. * indicates phases assumed to be present but consumed during later metamorphism. [1] Tack et al. (2010). [2] Monteyne-Poulaert et al. (1962); Dewaele et al. (2011, 2016); De Clercq (2012); Melcher et al. (2015) and Zhang et al. (2016). [3] Van Daele and Scherer (in revision). [4] Eyles (2008); Fernandez-Alonso et al. (2012). [5] Midende et al. (2014); Decrée et al. (2019). [6] Oriolo et al. (2016, 2017). (For interpretation of the references to color in this figure legend, the reader is referred to the Web version of this article.)

6.4. Retrograde metamorphism

Chlorite type 3 from retrograde metamorphism can be petrographically distinguished from regional and contact metamorphic chlorite because of its heterogeneous texture and internal biotite relicts (Fig. 4b and n). Two retrograde chlorite samples (KG96 and 122) show constrained temperatures of 459 ± 12 °C and 437 ± 26 °C, respectively. The two other samples analyzed (KG07 and 125) show highly variable temperatures up to *c.* 625 °C, similar to the maximum temperatures obtained for chlorites of type 1 and 2 (Table 4). The geochemical composition of chlorite in these two samples therefore is interpreted to only partially represent the retrograde conditions and an average value of *c.* 450 °C (based on KG96 and 122) is assumed for the retrograde metamorphism. This temperature is lower than the regional M3 temperature of *c.* 520 °C. Greenschist facies retrograde metamorphism was reported for the KAB, inducing both sericitization and chloritization (Nahimana, 1988; Rumvegeri, 1991; Prochaska et al., 1992; Börker and Pupp, 2014). The additional occurrence of kaolinite, sericite, and white mica pseudomorphs in lenses as part of the retrograde assemblage suggests abundant fluid flow at retrograde conditions (e.g. Yardley and Baltatzis, 1985).

6.5. Temperature evolution in the Kibuye-Gitarama-Gatumba area

With the petrographic and analytical results of this study, the temperature evolution during the Late Mesoproterozoic and Neoproterozoic in the Western Domain of the Karagwe-Ankole Belt can be reconstructed. Geochronological data from literature allow to add an absolute time parameter to the geothermometric data (Fig. 7). As mentioned in the introduction, granite-related Nb–Ta–Sn–W mineralization (pegmatites, quartz veins) was emplaced in Rwanda during the period 998–957 Ma (Monteyne-Poulaert et al., 1962; Brinckmann et al., 2001; Dewaele et al., 2011, 2016; De Clercq, 2012; Melcher et al., 2015; Zhang et al., 2016) at a post-compressional (D1) stage (Hulsbosch et al., 2017). Metasomatic and contact metamorphic events associated with the granite magmatism and pegmatites are hence expected to have an Early Neoproterozoic timing (*c.* 1000–960 Ma). In addition, Lu–Hf garnet geochronology from the Gatumba area gives two garnet growth episodes, i.e. one older than 920 Ma and one around 880 Ma (Fig. 7), while post-deformational garnets from the Kibuye area show Lu–Hf dates between 618.9 ± 1.6 and 602.3 ± 1.1 Ma (Van Daele & Scherer, *in revision*). These results are interpreted to represent the timing of M1, M2 and M3 metamorphism respectively. Concordant U–Pb ages of metamorphic apatite between 596 and 541 Ma confirm the Ediacaran (635–541 Ma) metamorphic event (Van Daele et al., *in revision*). To our knowledge, no ages were determined for Neoproterozoic deformation or retrograde metamorphism in the KAB yet. The Neoproterozoic D2 event can be constrained between 880 Ma (youngest pre-D2 garnet) and 620 Ma (oldest undeformed, i.e. post-D2, garnet; Van Daele & Scherer, *in revision*).

In metasiltstones, the assemblages biotite–white mica–garnet ± staurolite(–chlorite) and kyanite–biotite(–white mica–chlorite) were stable during M1 peak metamorphic conditions. Likewise, the prograde (sub-)greenschist metamorphic minerals (e.g. albite, graphite, biotite) form part of the prograde Barrovian P–T path during the Mesoproterozoic (Fig. 7). During pre-D2 metamorphism (M1–M2), amphibolite facies peak conditions lead to the crystallization of hornblende, calcic feldspar ($> An_{24}$) and titanite, converting the diorites into amphibolites. Only a few garnet–biotite mineral pairs and chlorite crystals in the metasediments and amphibolites have preserved their original M1–M2 signature, suggesting that a temperature of up to 630 °C was reached at the end of the Mesoproterozoic – start of the Neoproterozoic (Tables 3 and 4).

At the end of the Mesoproterozoic, a major first deformational event D1 took place before the intrusion of the G4 leucogranites and pegmatites, as indicated by their occurrence in fold hinges, axial plane foliations (S_{f2}) and anticline cores during a post-compressional regime (Hulsbosch et al., 2017). At the start of the Neoproterozoic, granite contact metamorphism and metasomatism took place during or closely following the granite and pegmatite intrusions. Antigorite indicates hydrothermal activity, likely genetically linked to the granites, took place under a temperature regime between 250 and 600 °C.

The D2 deformation event had minor influence as indicated by the relatively undeformed pegmatites; it probably reinforced the structures and S_{f2}-foliations previously developed during D1, and only locally formed the S_{f3}-foliation. Similar reactivation has been observed for mylonitic fabrics in the Ubendian Belt (Boniface et al., 2012).

Most garnet–biotite pairs, as well as chlorite, were geochemically reset during the younger, post-deformational metamorphic regime in the KGG area (M3). This is especially evidenced by the large spread observed in the chlorite data (Table 4). The M3 greenschist facies metamorphism with a temperature of *c.* 525 °C took place in the KGG area around *c.* 610 Ma (Van Daele and Scherer, *in revision*). The mineral assemblage observed in metapelites consists of garnet–biotite–white mica(–chlorite). The amphibolite facies assemblage in mafic rocks was partially reset at high-T greenschist facies conditions as well. Hornblende, biotite and epidote (re-)crystallized at a post-D2 stage, while retrograde albitization of the calcic feldspar was limited.

Lastly, the rocks were affected by retrograde metamorphism which induced biotite chloritization at *c.* 450 °C. Other retrograde effects, not necessarily simultaneous, are sericitization and kaolinitization of feldspar, and white mica pseudomorphism of staurolite and/or kyanite. This retrograde metamoprhism could correspond with the hydrothermal activity in the area as widely accepted in literature to have occurred at *c.* 550 Ma (Cahen et al., 1984; Dewaele et al., 2011; Melcher et al., 2015).

6.6. Relation between tectono-metamorphism and the geodynamic framework

The D1 deformational event shaped the regional geometry of the Western Domain of the KAB, induced NW–SE to NNE–SSW trending upright folding and foliation development in the metasediments and has been linked to the Late Mesoproterozoic Rodinia amalgamation (Klerkx et al., 1984; Rumvegeri, 1991; Fernandez-Alonso and Theunissen, 1998; Fernandez-Alonso et al., 2012). No clear indications for sudden drops or rises in temperature during the Neoproterozoic were found in the petrographic record nor in the results of the geothermometric study. Only limited and local sedimentation (the Itombwe Supergroup) has been determined during the Neoproterozoic in the WD (Fernandez-Alonso et al., 2012). In the KGG area, no indications for multiple sediment deposition or uplift and erosion episodes during the Neoproterozoic have been observed in the lithological record, which could have induced substantial cooling and reheating between the M1–M2 and M3 metamorphic events. The M2 event (*c.* 880 Ma) is time-equivalent to the start of rifting and ocean development during the Rodinia break-up as indicated by the ophiolite remnants observed in the Lufilian and Zambezi Belts in Zambia (John et al., 2004; De Waele et al., 2008) although a causal link cannot be proven. The extensional setting in the KAB due to Rodinia break-up in the period 800–700 Ma (Midende et al., 2014) corresponds to and can be considered as a far field effect of the intraplate continental rifting observed in the Congo Craton from 830 to 745 Ma, and the superplume activity under the Arabian-Nubian shield in the period 850–750 Ma (Li et al., 2008) and likely had an increasing influence on the temperature regime in the KAB.

Thereafter, the amalgamation of Gondwana dominated the geodynamic regime, with as culmination the collisional events around 630–600 Ma in the Congo Craton west of the study area ('West-Gondwana orogeny'; Oriolo et al., 2017), and the continent-continent collision around 650–615 Ma between Azania and East-Africa east of the study area ('East-African Orogeny'; Fritz et al., 2013). The expression of these far-field effects can be found in the KAB as the youngest D2 deformation event and post-D2 greenschist-facies M3 metamorphism. The minor D2 event probably corresponds to the NS-oriented Pan-African overprint at the end of the Ediacaran (Fernandez-Alonso et al., 2012). The third metamorphic M3 pulse temporally corresponds with the Neoproterozoic tectonometamorphic reworking of the Paleoproterozoic Ubendian Belt which is related to the Gondwana Supercontinent assembly as well (Fig. 2; Boniface and Appel, 2018).

The temperature reconstruction for the Kibuye-Gitarama-Gatumba area suggests that a high temperature prevailed in the Western Domain of the Karagwe-Ankole Belt at the end of the Mesoproterozoic and throughout most of the Neoproterozoic. Closure temperatures for biotite vary, depending on cooling rate and crystal size, between 280 and 345 °C for Ar (Harrison et al., 1985) and 300–400 °C for the Rb–Sr system (Jenkin et al., 2001; Willigers et al., 2004). For muscovite, isotopic closure can already be reached at slightly higher temperatures: 270–450 °C for Ar (Hames and Bowring, 1994; Harrison et al., 2009; Scharf et al., 2016) and even 500–550 °C for Sr (van Blanckenburg et al., 1989; Freeman et al., 1997; Eberlei et al., 2015). A regional temperature of 520 °C significantly exceeds these values, except for the Rb–Sr system in muscovite, of which the closure temperature only partly overlaps. This comparison demonstrates the possibility of long-term thermal diffusion of radiogenic isotopes (e.g. ^{87}Sr, ^{40}Ar) in phyllosilicates, which should be taken into account when interpreting geochronological results. The obtained temperature reconstruction (Fig. 7) offers an explanation for the Ediacaran and Cambrian Ar–Ar and Rb–Sr phyllosilicate dates obtained in the Western Domain of the Karagwe-Ankole Belt, the large geochronological variation observed on a local scale and the lack of association between these geochronological results and geological events (e.g. Dewaele et al., 2011; Van Daele et al., 2018b).

7. Conclusion

In the Western Domain of the Karagwe-Ankole Belt, prograde Barrovian-type metamorphism with peak metamorphism at amphibolite facies conditions (up to *c.* 630 °C) during the Meso- and Early Neoproterozoic was followed by extended post-deformational greenschist facies metamorphism (T = *c.* 525 °C to *c.* 440 °C) at the end of the Neoproterozoic. Metasiltstone from the Kibuye-Gitarama-Gatumba area preserves relicts of the prograde Barrovian-type metamorphic evolution up to amphibolite facies conditions (biotite, albite, graphite, chlorite, white mica, garnet, staurolite and kyanite), but also records post-deformational re-equilibration towards greenschist facies conditions (garnet, biotite, white mica, chlorite). In contrast, amphibolites show, except for the presence of calcic feldspar, no evidence for the prograde part of the metamorphic cycle that affected the area. The minerals hornblende, biotite and epidote mainly reflect the Late Neoproterozoic greenschist metamorphism.

The metamorphic history of the KAB as proposed here based on petrography and quantitative geothermometry fits very well in the geodynamic framework of the surrounding terranes; i.e. the assembly of the Rodinia supercontinent at *c.* 1.0 Ga (M1, D1), followed by its break-up in the period 800–700 Ma (M2?) and the formation of the Gondwana supercontinent at the end of the Neoproterozoic (D2, M3). The quantitative temperature evolution obtained in this study, supported by the geochronological framework, indicates temperatures > 500 °C were reached regionally at the start and end of the Neoproterozoic, which is an important factor to be taken into account in the interpretation of thermal diffusion-sensitive geochronological data.

Funding

Johanna Van Daele is a research assistant of the Research Foundation – Flanders (FWO). Research of Niels Hulsbosch is funded by a postdoctoral fellowship of the FWO. Field work was supported by a grant from the Dirk Vogel Fund. Additional financial support from the research grant C14/17/056 of the KU Leuven Special Research Fund is especially acknowledged.

Declaration of competing interest

The authors declare that they have no known competing financial interests or personal relationships that could have appeared to influence the work reported in this paper.

Acknowledgments

Dr. Emmanuel Munyengabe, Dr. Michael Biryabarema, Mr. Francis Gatare and Mr. Alain Ntenge of the Rwanda Mines, Petroleum and Gas Board are thanked for the authorization to conduct field work in Rwanda and to export the samples. We also would like to express our gratitude to Mr. Herman Nijs (KU Leuven) for preparing the high-quality thin sections and to Mr. Pieter L'hoëst (KU Leuven) for his explanation and guidance with the FEG-EPMA. Editor Damien Delvaux is thanked for his editorial handling of the manuscript. Constructive feedback from two anonymous reviewers significantly improved the manuscript and is greatly appreciated.

Appendix A. Supplementary data

Supplementary data to this article can be found online at https://doi.org/10.1016/j.jafrearsci.2020.103783.

References

Best, M.G., 2002. Igneous and Metamorphic Petrology, second ed. Blackwell Science Ltd.
Boniface, N., Appel, P., 2018. Neoproterozoic reworking of the ubendian belt crust: implication for an orogenic cycle between the Tanzania craton and bangweulu block during the assembly of Gondwana. Precambrian Res. 305, 358–385. https://doi.org/10.1016/j.precamres.2017.12.011.
Boniface, N., Schenk, V., Appel, P., 2012. Paleoproterozoic eclogites of MORB-type chemistry and three Proterozoic orogenic cycles in the Ubendian Belt (Tanzania): evidence from monazite and zircon geochronology, and geochemistry. Precambrian Res. 192– 195, 16–33. https://doi.org/10.1016/j.precamres.2011.10.007.
Börker, J., Pupp, M., 2014. Geology of the Gatumba Area, Rwanda. Unpubl. Masterthesis. Clausthal University of Technology.
Bourdelle, F., Parra, T., Chopin, C., Beyssac, O., 2013. A new chlorite geothermometer for diagenetic to low-grade metamorphic conditions. Contrib. Mineral. Petrol. 165, 723–735. https://doi.org/10.1007/s00410-012-0832-7.
Brinckmann, J., Lehmann, B., Hein, U., Höhndorf, A., Mussallam, K., Weiser, T., Timm, F., 2001. La géologie et la minéralisation primaire de l'or de la Chaîne Kibarienne, nord-ouest du Burundi, Afrique orientale. Geol. Jahrbuch Reihe E Geophys. 101, 3–195.
Buchwaldt, R., Toulkeridis, T., Todt, W., Ucakuwun, E.K., 2008. Crustal age domains in the Kibaran belt of SW-Uganda: combined zircon geochronology and Sm–Nd isotopic investigation. J. Afr. Earth Sci. 51, 4–20. https://doi.org/10.1016/j.jafrearsci.2007.11.001.
Butler, R.W.H., Torvela, T., 2018. The competition between rates of deformation and solidification in syn-kinematic granitic intrusions: resolving the pegmatite paradox. J. Struct. Geol. 117, 1–13. https://doi.org/10.1016/j.jsg.2018.08.013.
Cahen, L., Snelling, N., Delhal, J., Vail, J., Bonhomme, M., Ledent, D., 1984. The Geochronology and Evolution of Africa. Oxford University Press, Oxford.
Cathelineau, M., 1988. Cation site occupancy in Chlorite and Illites as a function of temperature. Clay Miner. 23, 471–485.
De Clercq, F., 2012. Metallogenesis of Sn and W Vein-type Deposits in the Karagwe-Ankole Belt (Rwanda). Unpubl. PhD thesis. KU Leuven.
de Kock, G.S., Dhansay, T., Armstrong, R., 2014. Akanyaru-Ankole Supergroup of Rwanda: strata, structures and ages. In: Boniface, N. (Ed.), Abstracts Volume: 25th Colloquium of African Geology. Tanzania Geological Society, Dar Es Salaam, Tanzania, pp. 2.
De Waele, B., Johnson, S.P., Pisarevsky, S.A., 2008. Palaeoproterozoic to Neoproterozoic growth and evolution of the eastern Congo Craton: its role in the Rodinia puzzle. Precambrian Res. 160, 127–141. https://doi.org/10.1016/j.precamres.2007.04.020.
Deblond, A., Punzalan, L.E., Boven, A., Tack, L., 2001. The Malagarazi Supergroup of southeast Burundi and its correlative Bukoba Supergroup of Northwest Tanzania: neo- and Mesoproterozoic chronostratigraphic constraints from Ar-Ar ages on mafic intrusive rocks. J. Afr. Earth Sci. 32, 435–449. https://doi.org/10.1016/S0899-5362(01)90107-1.
Debruyne, D., Hulsbosch, N., Van Wilderode, J., Balcaen, L., Vanhaecke, F., Muchez, P., 2015. Regional geodynamic context for the mesoproterozoic Kibara belt (KIB) and the karagwe-ankole belt: evidence from geochemistry and isotopes in the KIB. Precambrian Res. 264, 82–97. https://doi.org/10.1016/j.precamres.2015.04.001.
Decrée, S., Demaiffe, D., Tack, L., Nimpagaritse, G., De Paepe, P., Boulvais, P., Debaille, V., 2019. The Neoproterozoic Upper Ruvubu alkaline plutonic complex (Burundi) revisited: large-scale syntectonic emplacement, magmatic differentiation and late-stage circulations of fluids. Precambrian Res. 325, 150–171. https://doi.org/10.1016/j.precamres.2019.02.023.
Dehandschutter, J., Buyagu, S., Theunissen, K., Baudet, S., Delhaye, F., Fernandez-Alonso, M., De Mulder, M., Mattheussens, M., Meulemans, H., Peeters, L., Salée, A., Tréfois, P., 1988. Carte Géologique du Rwanda, Feuille Kibuye, 1:100,000 et note explicative. Département de Géologie et de Minéralogie du Musée royal de l'Afrique Centrale (Belgium) and the Ministère de l'Industrie et de l'Artisanat du Rwanda.
Dewaele, S., De Clercq, F., Hulsbosch, N., Piessens, K., Boyce, A., Burgess, R., Muchez, P., 2016. Genesis of the vein-type tungsten mineralization at nyakabingo (Rwanda) in the karagwe–ankole belt, central Africa. Miner. Depos. 51, 283–307. https://doi.org/10.1007/s00126-015-0608-x.
Dewaele, S., Henjes-Kunst, F., Melcher, F., Sitnikova, M., Burgess, R., Gerdes, A., Fernandez-Alonso, M., De Clercq, F., Muchez, P., Lehmann, B., 2011. Late Neoproterozoic overprinting of the cassiterite and columbite-tantalite bearing pegmatites of the Gatumba area, Rwanda (Central Africa). J. Afr. Earth Sci. 61, 10–26. https://doi.org/10.1016/j.jafrearsci.2011.04.004.
Eberlei, T., Habler, G., Wegner, W., Schuster, R., Körner, W., Thöni, M., Abart, R., 2015. Rb/Sr isotopic and compositional retentivity of muscovite during deformation. Lithos 227, 161–178. https://doi.org/10.1016/j.lithos.2015.04.007.
Evans, B.W., 2004. The serpentinite multisystem revisited: chrysotile is metastable. Int. Geol. Rev. 46, 479–506.
Eyles, N., 2008. Glacio-epochs and the supercontinent cycle after ~3.0 Ga: tectonic boundary conditions for glaciation. Palaeogeogr. Palaeoclimatol. Palaeoecol. 258, 89–129. https://doi.org/10.1016/j.palaeo.2007.09.021.
Fernandez-Alonso, M., Cutten, H., De Waele, B., Tack, L., Tahon, A., Baudet, D., Barritt, S.D., 2012. The Mesoproterozoic Karagwe-Ankole Belt (formerly the NE Kibara Belt): the result of prolonged extensional intracratonic basin development punctuated by two short-lived far-field compressional events. Precambrian Res. 216–219, 63–86. https://doi.org/10.1016/j.precamres.2012.06.007.
Fernandez-Alonso, M., Lavreau, J., Klerkx, J., 1986. Geochemistry and geochronology of the kibaran granites in Burundi, central Africa: implications for the kibaran orogeny. Chem. Geol. 57, 217–234. https://doi.org/10.1016/0009-2541(86)90104-X.
Fernandez-Alonso, M., Tack, L., Tahon, A., 2007. Geological map of the mesoproterozoic northeastern kibara belt. 1 500.000.
Fernandez-Alonso, M., Theunissen, K., 1998. Airborne geophysics and geochemistry provide new insights in the intracontinental evolution of the Mesoproterozoic Kibaran belt (Central Africa). Geol. Mag. 135, 203–216. https://doi.org/10.1017/S0016756898008310.
Ferry, J.M., Spear, F.S., 1978. Calibrage expérimental du partage du fer (Fe) et du magnésium (Mg) entre la Biotite et le Grenat. Contrib. Mineral. Petrol. 66, 113–117.
Freeman, S.R., Inger, S., Butler, R.W.H., Cliff, R.A., 1997. Dating deformation using Rb-Sr in white mica: greenschist facies deformation ages from the Entrelor shear zone, Italian Alps. Tectonics 16, 57–76. https://doi.org/10.1029/96TC02477.
Fritz, H., Abdelsalam, M., Ali, K.A., Bingen, B., Collins, A.S., Fowler, A.R., Ghebreab, W., Hauzenberger, C.A., Johnson, P.R., Kusky, T.M., Macey, P., Muhongo, S., Stern, R.J., Viola, G., 2013. Orogen styles in the east african orogen: a review of the neoproterozoic to cambrian tectonic evolution. J. Afr. Earth Sci. 86, 65–106. https://doi.org/10.1016/j.jafrearsci.2013.06.004.
Gérards, J., 1965. Géologie de la région de Gatumba. Bull. du Serv. Géologique Rwandaise 2, 31–42.
Hames, W.E., Bowring, S.A., 1994. An empirical evaluation of the argon diffusion geometry in muscovite. Earth Planet Sci. Lett. 124, 161–167. https://doi.org/10.1016/0012-821X(94)00079-4.
Harrison, T.M., Célérier, J., Aikman, A.B., Hermann, J., Heizler, M.T., 2009. Diffusion of 40Ar in muscovite. Geochem. Cosmochim. Acta 73, 1039–1051. https://doi.org/10.1016/j.gca.2008.09.038.
Harrison, T.M., Duncan, I., McDougall, I., 1985. Diffusion of 40Ar in biotite: temperature, pressure and compositional effects. Geochem. Cosmochim. Acta 49, 2461–2468. https://doi.org/10.1016/0016-7037(85)90246-7.
Hey, M.H., 1954. A new review of the chlorites. J. Mineral. Soc. 30, 277–292.
Hillier, S., Velde, B., 1991. Octahedral occupancy and the chemical composition of diagenetic (Low-Temperature) chlorites. Clay Miner. 26, 149–168. https://doi.org/10.1180/claymin.1991.026.2.01.
Hoinkes, G., 1986. Effect of grossular-content in garnet on the partitioning of Fe and Mg between garnet and biotite. Contrib. Mineral. Petrol. 92, 393–399.
Hulsbosch, N., Boiron, M.-C., Dewaele, S., Muchez, P., 2016. Fluid fractionation of tungsten during granite–pegmatite differentiation and the metal source of peri-batholitic W quartz veins: evidence from the Karagwe-Ankole Belt (Rwanda). Geochem. Cosmochim. Acta 175, 299–318. https://doi.org/10.1016/j.gca.2015.11.020.
Hulsbosch, N., Hertogen, J., Dewaele, S., André, L., Muchez, P., 2014. Alkali metal and rare earth element evolution of rock-forming minerals from the Gatumba area pegmatites (Rwanda): quantitative assessment of crystal-melt fractionation in the regional zonation of pegmatite groups. Geochem. Cosmochim. Acta 132, 349–374. https://doi.org/10.1016/j.gca.2014.02.006.
Hulsbosch, N., Muchez, P., 2019. Tracing Fluid Saturation during Pegmatite Differentiation by Studying the Fluid Inclusion Evolution and Multiphase Cassiterite Mineralisation of the Gatumba Pegmatite Dyke System (NW Rwanda). Lithos in press.
Hulsbosch, N., Van Daele, J., Reinders, N., Dewaele, S., Jacques, D., Muchez, P., 2017. Structural control on the emplacement of contemporaneous Nb-Ta-Sn pegmatite intrusions and Sn quartz veins: insights from the Musha and Ntunga deposits of the Karagwe-Ankole Belt. Rwanda. J. African Earth Sci. 137, 24–32.
Jenkin, G.R.T., Ellam, R.M., Rogers, G., Stuart, F.M., 2001. An investigation of closure temperature of the biotite Rb-Sr system: the important of cation exchange. Geochem. Cosmochim. Acta 65, 1141–1160. https://doi.org/10.1016/S0016-7037(00)00560-3.
John, T., Schenk, V., Mezger, K., Tembo, F., 2004. Timing and PT evolution of whiteschist metamorphism in the lufilian arc-zambezi belt orogen (Zambia): implications for the assembly of Gondwana. J. Geol. 112, 71–90. https://doi.org/10.1086/379693.

Jowett, E.C., 1991. Fitting iron and magnesium into the hydrothermal chlorite geothermometer. In: Geol. Assoc. Canada/Mineral. Assoc. Canada/Soc. Econ. Geol. Joint Annual Meeting - Program with Abstracts 16. Toronto, pp. A62.
Klein, C., Dutrow, B., O'Callaghan, Jay, 2007. The Manual of Mineral Science, 23rd ed. John Wiley & Sons, Inc.
Klerkx, J., Liégeois, J.P., Lavreau, J., Claessens, W., 1987. Crustal evolution of the northern Kibara Belt, eastern and central Africa. In: Kröner, A. (Ed.), Proterozoic Lithospheric Evolution. American Geophysical Union and the Geological Society of America, pp. 217–233.
Klerkx, J., Liégeois, J.P., Lavreau, J., Theunissen, K., 1984. Granitoides kibariens précoces et tectonique tangentielle au Burundi: magmatisme bimodal lié a une distention crustale. In: Klerckx, J., Michot, J. (Eds.), African Geology, A Volume in Honour of L. Cahen. Royal Museum for Central Africa, Tervuren, pp. 29–46.
Koegelenberg, C., Kisters, A.F.M., 2014. Tectonic wedging, back-thrusting and basin development in the frontal parts of the Mesoproterozoic Karagwe-Ankole belt in NW Tanzania. J. Afr. Earth Sci. 97, 87–98. https://doi.org/10.1016/j.jafrearsci.2014.04.018.
Koegelenberg, C., Kisters, A.F.M., Kramers, J.D., Frei, D., 2015. U-Pb detrital zircon and 39Ar-40Ar muscovite ages from the eastern parts of the Karagwe-Ankole Belt: tracking Paleoproterozoic basin formation and Mesoproterozoic crustal amalgamation along the western margin of the Tanzania Craton. Precambrian Res. 269, 147–161. https://doi.org/10.1016/j.precamres.2015.08.014.
Kohn, M., 2003. Geochemical zoning in metamorphic minerals. In: Rudnick, R.L. (Ed.), Treatise on Geochemistry. Elsevier, pp. 229–261.
Kokonyangi, J., Armstrong, R., Kampunzu, A.B., Yoshida, M., Okudaira, T., 2004. U-Pb zircon geochronology and petrology of granitoids from Mitwaba (Katanga, Congo): implications for the evolution of the Mesoproterozoic Kibaran belt. Precambrian Res. 132, 79–106. https://doi.org/10.1016/j.precamres.2004.02.007.
Kokonyangi, J., Kampunzu, A.B., Poujol, M., Okudaira, T., Yoshida, M., Shabeer, K.P., 2005. Petrology and geochronology of mesoproterozoic mafic-intermediate plutonic rocks from mitwaba (D. R. Congo): implications for the evolution of the kibaran belt in central Africa. Geol. Mag. 142, 109–130. https://doi.org/10.1017/S0016756804009951.
Kokonyangi, J., Okudiaira, T., Kampunzu, A.B., Yoshida, M., 2001. Geological evolution of the kibarides belt, mitwaba, democratic republic of Congo, central Africa. Gondwana Res. 4, 663–664.
Kokonyangi, J.W., Kampunzu, A.B., Armstrong, R., Arima, M., Yoshida, M., Okudaira, T., 2007. U-Pb SHRIMP dating of detrital zircons from the Nzilo Group (Kibaran belt): implications for the source of sediments and Mesoproterozoic evolution of Central Africa. J. Geol. 115, 99–113. https://doi.org/10.1086/509270.
Kokonyangi, J.W., Kampunzu, A.B., Armstrong, R., Yoshida, M., Okudaira, T., Arima, M., Ngulube, D.A., 2006. The mesoproterozoic kibaride belt (katanga, SE D.R. Congo). J. Afr. Earth Sci. 46, 1–35. https://doi.org/10.1016/j.jafrearsci.2006.01.017.
Lanari, P., Guillot, S., Schwartz, S., Vidal, O., Riel, N., Beyssac, O., Lanari, P., Guillot, S., Schwartz, S., Vidal, O., Tricart, P., 2012. Diachronous evolution of the alpine continental subduction wedge: evidence from P-T estimates in the Briançonnais Zone houillère (France - western Alps). J. Geodyn. 56–57, 39–54.
Lanari, P., Wagner, T., Vidal, O., 2014. A thermodynamic model for di-trioctahedral chlorite from experimental and natural data in the system MgO – FeO – Al2O3 – SiO2 – H2O : applications to P – T sections and geothermometry. Contrib. Mineral. Petrol. 167, 19. https://doi.org/10.1007/s00410-014-0968-8.
Lehmann, B., Halder, S., Ruzindana Munana, J., de la Paix Ngizimana, J., Biryabarema, M., 2014. The geochemical signature of rare-metal pegmatites in Central Africa: magmatic rocks in the Gatumba tin–tantalum mining district, Rwanda. J. Geochem. Explor. 144, 528–538. https://doi.org/10.1016/j.gexplo.2013.11.012.
Li, Z.X., Bogdanova, S.V., Collins, A.S., Davidson, A., De Waele, B., Ernst, R.E., Fitzsimons, I.C.W., Fuck, R.A., Gladkochub, D.P., Jacobs, J., Karlstrom, K.E., Lu, S., Natapov, L.M., Pease, V., Pisarevsky, S.A., Thrane, K., Vernikovsky, V., 2008. Assembly, configuration, and break-up history of Rodinia: a synthesis. Precambrian Res. 160, 179–210. https://doi.org/10.1016/j.precamres.2007.04.021.
Melcher, F., Graupner, T., Gäbler, H.E., Sitnikova, M., Henjes-Kunst, F., Oberthür, T., Gerdes, A., Dewaele, S., 2015. Tantalum-(niobium-tin) mineralisation in African pegmatites and rare metal granites: constraints from Ta-Nb oxide mineralogy, geochemistry and U-Pb geochronology. Ore Geol. Rev. 64, 667–719. https://doi.org/10.1016/j.oregeorev.2013.09.003.
Midende, G., Boulvais, P., Tack, L., Melcher, F., Gerdes, A., Dewaele, S., Demaiffe, D., Decrée, S., 2014. Petrography, geochemistry and U-Pb zircon age of the matongo carbonatite massif (Burundi): implication for the neoproterozoic geodynamic evolution of central Africa. J. Afr. Earth Sci. 100, 656–674. https://doi.org/10.1016/j.jafrearsci.2014.08.010.
Monteyne-Poulaert, G., Delwiche, R., Safianikoff, A., Cahen, L., 1962. Age de minéralisations pegmatitiques et. filoniennes du Rwanda et du Burundi 71, 272–295.
Nahimana, L., 1988. Métamorphisme, tectonique et magmatisme dans une portion de la chaîne kibarienne du Nord-Ouest du Burundi. Unpubl. PhD thesis. Université Catholique de Louvain.
Oriolo, S., Oyhantçabal, P., Wemmer, K., Heidelbach, F., Pfänder, J., Basei, M.A.S., Hueck, M., Hannich, F., Sperner, B., Siegesmund, S., 2016. Shear zone evolution and timing of deformation in the Neoproterozoic transpressional Dom Feliciano Belt, Uruguay. J. Struct. Geol. 92, 59–78. https://doi.org/10.1016/j.jsg.2016.09.010.
Oriolo, S., Oyhantçabal, P., Wemmer, K., Siegesmund, S., 2017. Contemporaneous assembly of Western Gondwana and final Rodinia break-up: implications for the supercontinent cycle. Geosci. Front. 8, 1431–1445. https://doi.org/10.1016/j.gsf.2017.01.009.
Parra, T., Vidal, O., Theye, T., 2005. Experimental data on the Tschermak substitution in Fe-chlorite. Am. Mineral. 90, 359–370. https://doi.org/10.2138/am.2005.1556.
Pohl, W.L., 1988. "Post-orogenic" events within and nearby the Kibara belt in central Africa. Int. Geol. Correl. Program. Proj. n° 255 1, 47–50.
Pohl, W.L., Biryabarema, M., Lehmann, B., 2013. Early Neoproterozoic rare metal (Sn, Ta Inst., W) and gold metallogeny of Central Africa: a review. B. Appl. Earth Sci. 122, 66–82.
Prochaska, W., Mogessie, A., Raith, J.G., 1992. Formation of the talc deposit of Kibanda (Rwanda) and its relation to the regional metamorphic evolution. J. Afr. Earth Sci. 14, 499–509.
Rumvegeri, B.T., 1991. Tectonic significance of kibaran structures in central and eastern Africa. J. Afr. Earth Sci. 13, 267–276. https://doi.org/10.1016/0899-5362(91)90010-V.
Scharf, A., Handy, M.R., Schmid, S.M., Favaro, S., Sudo, M., Schuster, R., Hammerschmidt, K., 2016. Grain-size effects on the closure temperature of white mica in a crustal-scale extensional shear zone - implications of in-situ 40Ar/39Ar laser-ablation of white mica for dating shearing and cooling (Tauern Window, Eastern Alps). Tectonophysics 674, 210–226. https://doi.org/10.1016/j.tecto.2016.02.014.
Siivola, J., Schmid, R., 2007. Recommendations by the IUGS subcommision on the systematics of metamorphic rocks: list of mineral abbreviations. Web Version 01.02.07. URL. http://www.bgs.ac.uk/scmr/docs/papers/paper_12.pdf accessed 10.22.19.
Tack, L., Liégeois, J.P., Deblond, a., Duchesne, J.C., 1994. Kibaran A-type granitoids and mafic rocks generated by two mantle sources in a late orogenic setting (Burundi). Precambrian Res. 68, 323–356. https://doi.org/10.1016/0301-9268(94)90036-1.
Tack, L., Wingate, M.T.D., De Waele, B., Meert, J., Belousova, E., Griffin, B., Tahon, A., Fernandez-Alonso, M., 2010. The 1375 Ma "Kibaran event" in Central Africa: prominent emplacement of bimodal magmatism under extensional regime. Precambrian Res. 180, 63–84. https://doi.org/10.1016/j.precamres.2010.02.022.
Tahon, A., Nsengiyumva, P., Antun, P., De Mulder, M., Theunissen, K., Baudet, S., Waleffe, A., Bertossa, A., Delhaye, F., Gerards, J., Lemonne, E., Mattheussens, M., Meulemans, H., Nzigimana, J., Peeters, L., Petricec, V., Salée, A., 1988a. Carte géologique du Rwanda, feuille Ruhengeri, 1:100,000 et note explicative. Département de Géologie et de Minéralogie du Musée royal de l'Afrique Centrale (Belgium) and the Ministère de l'Industrie et de l'Artisanat du Rwanda.
Tahon, A., Nsengiyumva, P., Dehandschutter, J., Buyagu, S., Mattheussens, M., Theunissen, K., Baudet, S., Delhaye, F., De Mulder, M., Meulemans, H., Peeters, L., Salée, A., Tréfois, P., 1988b. Carte géologique du Rwanda, feuille Nyabisindu, 1:100,000 et note explicative. Département de Géologie et de Minéralogie du Musée royal de l'Afrique Centrale (Belgium) and the Ministère de l'Industrie et de l'Artisanat du Rwanda.
Tindle, A., 2001a. Structural formula calculators (excel format) - chlorite. URL. http://www.open.ac.uk/earth-research/tindle/AGTWebPages/AGTSoft.html accessed 5.18.16.
Tindle, A., 2001b. Structural formula calculators (excel format) - biotite. URL. http://www.open.ac.uk/earth-research/tindle/AGTWebPages/AGTSoft.html accessed 5.18.16.
Tischendorf, G., Gottesmann, B., Förster, H.-J., Trumbull, R.B., 1997. On Li-bearing micas: estimating Li from electron microprobe analyses and an improved diagram for graphical representation. Mineral. Mag. 61, 809–834. https://doi.org/10.1180/minmag.1997.061.409.05.
van Blanckenburg, F., Villa, I.M., Baur, H., Morteani, G., Steiger, R.H., 1989. Time calibration of a PT-path from the western tauern window, eastern alps: the problem of closure temperatures. Contrib. Mineral. Petrol. 101, 1–11.
Van Daele, J., Dewaele, S., Melcher, F., Onuk, P., Spikings, R.A., Glorie, S., Jepson, G., Muchez, P., in Revision. Geochronology of Metamorphism, Deformation and Fluid Circulation: a Comparison between Rb-Sr and Ar-Ar Phyllosilicate and U-Pb Apatite Systematics in the Karagwe-Ankole Belt (Central Africa).
Van Daele, J., Hulsbosch, N., Dewaele, S., Boiron, M.-C., Piessens, K., Boyce, A., Muchez, P., 2018a. Mixing of magmatic-hydrothermal and metamorphic fluids and the origin of peribatholitic Sn vein-type deposits in Rwanda. Ore Geol. Rev. 101, 481–501.
Van Daele, J., Scherer, E.E., In Revision. Neoproterozoic Pre- and Post-deformational Metamorphism in the Western Domain of the Karagwe-Ankole Belt Reconstructed by Lu-Hf Garnet Geochronology in the Kibuye-Gatumba Area, Rwanda..
Van Daele, J., Spikings, R., Onuk, P., Melcher, F., Dewaele, S., Muchez, P., 2018b. Phyllosilicate Ar-Ar and Rb-Sr geochronology in the gitarama-gatumba area (Rwanda): an important neoproterozoic influence in the karagwe-ankole belt. In: 6th International Geologica Belgica Meeting 2018 Abstracts, pp. 2.
Vidal, O., Parra, T., Trotet, F., 2001. A thermodynamic model for Fe-Mg aluminous chlorite using data from phase equilibrium experiments and natural pelitic assemblages in the 100 to 600 °C, 1 to 25 kb range. Am. J. Sci. 301, 557–592.
Vidal, O., Parra, T., Vieillard, P., 2005. Thermodynamic properties of the Tschermak solid solution in Fe-chlorite: application to natural samples and possible role of oxidation. Am. Mineral. 90, 347–358. https://doi.org/10.2138/am.2005.1554.
Willigers, B.J.A., Mezger, K., Baker, J.A., 2004. Development of high precision Rb-Sr phlogopite and biotite geochronology; an alternative to 40Ar/39Ar tri-octahedral mica dating. Chem. Geol. 213, 339–358. https://doi.org/10.1016/j.chemgeo.2004.07.006.
Yardley, B.W.D., Baltatzis, E., 1985. Retrogression of staurolite schists and the sources of infiltrating fluids during metamorphism. Contrib. Mineral. Petrol. 89, 59–68.
Zane, A., Sassi, R., Guidotti, C.V., 1998. New data on metamorphic chlorite as a petrogenetic indicator mineral , with special regard to greenschist-facies rocks. Can. Mineral. 36, 713–726.
Zhang, R.Q., Sun, W.D., Lehmann, B., Seltmann, R., Li, C.Y., 2016. Multiple tin mineralization events in Africa: constraints by in-situ LA-ICPMS cassiterite U-PB ages. In: 35th International Geological Congress , Paper 2798. Cape Town, South Africa, pp. 2.